Universidad
Carlos III de Madrid

EXPERIMENTAL STUDY OF THE HEAT TRANSFER OF IMPINGING CHEVRON JETS

Andrés Felipe Betancourt Payán

Supervisor: Stefano Discetti

Universidad Carlos III
Bioengineering and Aerospace Engineering Department (EPS)
Leganés, Spain
2017

Acknowledgements

In a first place I would like to thank to my teachers (Stefano Discetti, Andrea Ianiro and Carlos Sanmiguel) for giving me the chance to carry out this project with them, giving advice, cheering me up and being available at any time I needed. Having them as tutors was much more than I could have asked for.

I am very thankful to all the people that directly or indirectly contributed to this project (university technicians and friends) by either helping with the instrumentation, giving me ideas to solve the problems I found and offering a hand when it was needed.

I would also like to thank my family for all the love and support during all this time and giving me the chance to complete this degree and present this work. The same way I would also like to thank to all my host families for making of me the resolute and strong person I am now, which helped me a lot for this thesis completion.

Abstract

In the present work, experimental results to show the impact in heat transfer of chevron impinging jets is going to be described. The object of study will be heat transfer coefficient, through the Nusselt number, of chevron impinging jets, by putting caps with different chevron configurations at the end of a nozzle. The parameters for the design of these caps are the number of chevron indentations (4 and 8), chevron length (4 and 8 mm) and chevron type (positive and negative). The technique used for the measurements is infrared thermography, making use of the heat flux sensor theory. Nusselt number maps are going to be obtained and discussed. The whole experimental set up and performance was carried out in the laboratory of the university, and the experimental set up and procedure is going to be explained in detail. The Reynolds number used for all experiments was 10000 and the nozzle exit was placed at distances 2, 4, 6 and 8 nozzle diameters. It will be seen, that certain chevron configurations show a better behavior than a standard circular nozzle, in some cases a 8-10% in heat transfer performance.

List of Symbols

Greek letter variables

α	Absorptivity	$-$
α_d	Thermal diffusivity	m^2/s
β	Volumetric thermal expansion coefficient	K^{-1}
ϵ	Emissivity	$-$
λ	Radiation wavelength	mm or μm
μ	Dynamic viscosity of the fluid	$N \cdot s/m^2$
ν	Radiation wave frequency	s^{-1}
ρ	Reflectivity	$-$
ρ_f	Density of the fluid	kg/m^3
τ	Transmissivity coefficient of the medium	$-$

Latin letter variables

Bi	Biot number	$-$
c_p	Heat capacity of fluid	J/K
c_o	Speed of light in vacuum	m/s
D	Nozzle diameter	mm
e	Energy of incident photon	J
E_a	Radiation intensity emitted by the surroundings (suppose blackbody)	W/m^2

E_b	Radiation intensity	W/m^s
$E_{b,a}$	Radiation intensity emitted by the ambient	W/m^s
$E_{b,atm}$	Radiation intensity emitted by the atmosphere	W/m^s
$E_{b,obj}$	Radiation intensity emitted by a blackbody at the same temperature	W/m^2
E_{gap}	Energy required for quantum level change	J
E_T	Total radiation intensity reaching the sensor	W/m^2
H	Distance from nozzle exit to impinging surface	mm
H/D	non-dimensional nozzle to plate distance	$-$
h	Convective heat transfer coefficient	W/m^2K
h_t	Total heat transfer coefficient	W/m^2K
k_f	Thermal conductivity of the fluid	W/mK
k_{plate}	Thermal conductivity of heated foil sensor	W/mK
L	Characteristic length	m
L_n	Nozzle length	mm
Nu	Nusselt Number	$-$
Nu_{mean}	Mean value of the Nusselt number	$-$
Nu_{std}	Standard deviation of the Nusselt number	$-$
q_{cond}	Conduction heat flux	W/m^2
$q_{cond,x}$	Conduction heat flux in the x-direction	W/m^2
$q_{cond,y}$	Conduction heat flux in the y-direction	W/m^2
q_{conv}	Convective heat flux	W/m^2
q_{Joule}	Heat flux by Joule effect	W/m^2
q_n	Natural convection heat flux	W/m^2
q_{rad}	Radiation heat flux	w/m^2
$r(x)$	Local nozzle radius	mm
r_i	Nozzle inlet radius	mm
r_o	Nozzle outlet radius	mm
r/D	Non-dimensional radial distance to stagnation point	$-$

Ra_L	Rayleigh number	$-$
Re	Reynolds number	$-$
s	Slab thickness	m
T	Absolute temperature	K
T_{cold}	Heat flux sensor temperature, power supply off	K
T_{hot}	Heat flux sensor temperature, power supply on	K
T_{film}	Temperature at a very thin region above the heated surface	K
T_{jet}	Jet temperature	K
T_r	Reference temperature	K
T_w	Wall/surface temperature	K
T_∞	Ambient fluid temperature	K
V	Fluid velocity	m/s
r_w	Distance to beginning of wall jet development	mm

Physical constants

σ	Stefan-Boltzmann constant	$5.670e^{-8} W/m^2K^4$
g	Gravity constant	$9.81 m/s^2$
$\hbar$	Planck's constant	$1.05e^{-34} J \cdot s$

List of Figures

2-1 Sketch of an impinging jet. 9

2-2 Absolute velocity magnitude distribution for the impinging jet flow and arrow field. Extracted from simulation Re 10000 and H/D = 2. 10

2-3 Axial velocity profiles from the axis symmetry axis at different distances from the impinged surface. 11

2-4 Radial velocity field. 12

2-5 Radial velocity profiles for at different distances from the stagnation point. 12

2-6 Maxima in the radial velocity for different distances from the stagnation point. 13

2-7 Nusselt number radial distributions for various nozzle-to-plate distances [23]. 14

2-8 B747 exhaust nozzles. 15

2-9 Details of the chevron geometry: length L and penetration depth p. [32] 16

2-10 Temporal sequence of instantaneous iso-surface axial velocity $W/W_j = 1.45$ (red in the circular jet) and 1.7 (purple in the chevron jet), azimuthal vorticity $\omega_\theta D_j/W_i = 4$ (cyan), axial vorticity $\omega_z D/Wj = -1.2$ (green) and 1.2 (yellow). Vectors on plane $Y/d = 0$. Time separation between snapshots $\Delta t W_j/D = 0.45$. [32]. 17

2-11 Chevron jet: contours of mean-axial velocity at different cross-sectional Z-planes; X-Y projection of velocity vectors. [33]. 17

3-1 Sketch of heated thin foil sensor. Diabatic back surface. 21

3-2 Buoyancy-driven flow over the bottom surface of a hot horizontal plate [5] 23

3-3 Printed circuit. [2] 25

4-1 Radiation cooling of a heated solid [5]. 27
4-2 Emission process [5]. 28
4-3 Spectrum of electromagnetic radiation [5]. 30
4-4 Radiation emitted by a surface [5]. 30
4-5 Characteristics of an isothermal blackbody cavity: Complete absorption, diffuse emission from an aperture and diffuse irradiation of interior surfaces [5]. 31
4-6 Comparison of blackbody and real surface emission [5]. 32
4-7 The absorption, reflection, and transmission of incident radiation by a semitransparent material. [11]. 33
4-8 Essential components of an IR scanner. [3] 34
4-9 Stirling cooler with the detector array (Courtesy of FLIR Systems, Inc.) [3] 36
4-10 Sketch of the radiation detected by the camera [9]. 37

5-1 Sketch of the experimental installation. 39
5-2 AWM720P1 Airfow meter. Image taken from product data sheet. 41
5-3 Pneumatic adjustments 42
5-4 Two-ring-clamp system. 43
5-5 Inner Vitoshinski nozzle shape. 45
5-6 3D printed Vitoshinski nozzle 45
5-7 Tested chevron taps. 47
5-8 Printed circuit board. 48
5-9 Mirror. 49

6-1 Sketch of the calibration set up. 52
6-2 Analytic curve vs. calculated points 54
6-3 Calibration of the massflowmeter. 54

7-1 Nusselt maps for the circular nozzle at different nozzle to plate distances. Re 10000. 58
7-2 Radial mean comparison for the circular nozzle at different H/D distances. Re 10000. 59
7-3 Nusselt maps for the different nozzle caps with negative chevron indentation at different nozzle to plate distances. Re 10000. . . . 61
7-4 Nusselt maps for the different nozzle caps with positive chevron (crown caps) at different nozzle to plate distances. Re 10000. . . . 62

7-5 Aximuthal along the radii for different nozzle heights. Re 10000. . 63

List of Tables

4-1 Summary of radiative properties. 33

5-1 Nozzle caps properties 46

7-1 Control parameters and their uncertainty 65

9-1 Summary of depreciation costs 69
9-2 Sumary of all electronic componets costs. 69
9-3 Sumary of all material costs. 70
9-4 Sumary of total costs. 71

Contents

Acknowledgements **ii**

Abstract **iii**

List of symbols **iv**

1 Introduction **2**

1.1 Impinging jets applications and economical importance 3

1.2 Heat transfer enhancement 4

1.3 Purpose of this work 6

1.4 Project planning 6

2 Impinging Jets **8**

2.1 Introduction to chevron nozzles 14

2.2 Parameters and geometry of chevron nozzles. 15

2.3 Jet development and differences between round and chevron nozzles. 16

2.3.1 Heat transfer 16

3 Heat Flux Sensors **19**

3.1 Heated Thin Foil Sensor 21

3.1.1 Natural Convection contribution 22

3.1.2 The printed circuit board. 24

3.1.3 Remarks 26

4 Radiation Theory and IR scanner **27**

4.1 Black Body Radiation 30

4.2 Other radiative Properties 33

4.3 IR scanner 34

4.4 Optical System 34
4.5 IR Temperature Detector 35
4.6 Cooler. 36
4.7 IR Scanner Performance 36
4.8 IR Scanner calibration 37

5 Experimental Set Up **39**
5.1 Pneumatic feeding 40
5.2 Test structure 43
5.2.1 The stagnation chamber 43
5.2.2 The Nozzle 44
5.2.3 Chevron Caps 45
5.2.4 Heated foil sensor and support 48
5.2.5 Mirror 49
5.3 Power supply and sensing 50

6 Experimental Procedure **51**
6.1 IR camera calibration 51
6.2 Massflowmeter calibration 54
6.3 Data Acquisition Process 55
6.4 Data processing 55
6.5 Data Results Analysis and Discussion 56

7 Results Analysis and Discussion. **57**
7.1 Circular nozzle. 57
7.2 Differences in chevron length. 59
7.3 Differences number of chevrons. 60
7.4 Azimuthal mean analysis. 60
7.5 Uncertainty estimation. 64

8 Symmary and Conslusions **66**

9 Project Budget **68**

10 Regulatory Framework **72**

11 Future Improvements **73**

Bibliography **75**

Bibliography **78**

Chapter 1

Introduction

Intensive studies on heat transfer can lead to the understanding of the impact of conduction, radiation and/or convection effects on scientific and technological applications. In the ongoing times, the society and the environment require more efficient and economic productions systems and means of transportation. To this end, it is of crucial importance to accurately measure the energy required to a certain end, while taking the most of the available/supplied energy.

In this work, convective cooling making use of impinging jets is going to be studied. Impinging jets have shown to be a very efficient device for thermal energy and mass transfer between a surface and a fluid. The first interests on impinging jets date from the sixties, when Gardon and Cobopue [16] first showed how the radial footprint of a single round impinging jet over a hot surface is strongly influenced by the dimensionless nozzle-to-plate distance H/D. Later on, further studies were carried out and it was found out that other parameters such as Reynolds number, the turbulence intensity and the angle of impingement also play an important role in this heat transfer system. Martin gathers results of all these parameters in a review paper [22].

1.1 Impinging jets applications and economical importance

Impinging jet installations have found their place in several industries because of their wide range of applications. In the *aerospace industry*, a very important application is the one of cooling down the leading edges of the first stages of turbines. For this, pressurized bleed flow (typically at 600°C after the compressor) is internally conducted to impinge the internal walls of the blade immersed in a very hot fluid (around 1400°C total temperature after passing the combustion chamber). Cooling down the turbine blades allows higher operation temperatures (and higher temperature ratios), which in terms of aircraft engines is translated into higher efficiency, higher turbine output per unit weight and reduction of fuel consumption. According to Zuckermann [35], this requires heat fluxes the order of magnitude of $1MW/m^2$.

It has to be taken into account that the implementation of such systems affects the structural strength and lifetime of the components (impinging jet cooling is more easily applied to turbine stator blades than to rotor blades). The same way, bleeding a fraction of air from the engine compressor entails a performance penalty and for this reason, a good knowledge of the system requirements and process capabilities will be needed by the designer.

Impinging jets have also been found to have a great potential in the *electronics industry*, since the thermal over stressing is one of the major causes of failure of electronic components, new high performance cooling systems are needed to cover the need of high heat transfer coefficients for every day more powerful components in more packed systems. Here the use of impinging jets happen to be more effective than the current fin and fan arrays [28]. An implementation example can be seen in the patent by Bartilson [4].

Jet impingement is also commonly used in several *industrial drying* operations involving rapid drying of materials in the form of continuous sheets (tissue paper, photographic film, textile) [26]. As drying rate is dictated by the rate of heat and mass transfer within the drying substrate and the surroundings, jet impingement results adequate when rapid drying or small equipment is desired. In comparison to traditional parallel flow drying, the use of impinging jets results in a higher

energy consumption and the possibility of burning the product due to overheating. For these reasons, during the design of an impinging jet dryer, it will be important to match the heat supply with the drying energy demand to avoid overheating and waste of energy [19].

Another application area is glass tempering [13], where again, effort to understand the relationship between the parameters involved in the impinging jets system designs is made, in order to optimize the appliance to the problem.

1.2 Heat transfer enhancement

Still, research to find other ways to improve heat transfer between the jet and impinged surface has been done. It is well known that intensity of turbulence is directly related to convection heat transfer, compromising somehow the effectiveness of the systems because of pressure losses. With the work done to date and the current studies, it is expected to develop more effective systems, able to increase heat transfer through an increment in turbulence while maintaining a low pressure drop. The orifice design is very important in jet impingement, since it will affect the pressure drop across the nozzle and the velocity profiles over the impinged surface. These velocity profiles will be related to the convective heat flux.

During the development of the jets, an entrainment mechanism takes place, which increments the impinging flow rate and is able to substantially increase the convective heat transport. For years, a lot of effort has been put on understanding this entrainment phenomenon and its mechanism, in order to be able to control it and optimize it.

Tennekes and Lumley [29] describe the *entrainment rate* as the rate at which the fluid from the jet becomes entangled or mixed with that from its surroundings as they join at the mixing layers. There have been many trials to increment this entrainment rate while having the pressure drop across the nozzle under control.

For non-circular jets, the so called *axis-switching* is main responsible mechanism of entrainment enhancement. This phenomenon can be seen in the laboratory and consists on a turn of the jet cross section as it spreads further away from

the orifice. According to [17], axis-switching is responsible, for example, of the enhanced large-scale entrainment in rectangular jets.

On the line of understanding the behavior of non-circular jets, Gulati [18] carried out a study of the influence of the nozzle shape on the local heat transfer distribution over a normally impinged air jet on a smooth flat surface. Carrying out experiments at different nozzle to plate distances and Reynolds numbers, they observed that although the heat transfer characteristic of square and circular jets are pretty similar, the Nusselt number distribution along the major and minor axis for the rectangular case is different. In addition, they found out that for a nozzle to plate distance up to 6 nozzle diameters, the Nusselt number distribution along the horizontal axis for rectangular jets is higher than in the stagnation region for circular and quadrangular jets.

Meslem [24] among others, went deeper into the problem and experimented with rectangular six-lobed orifices and compared the results with a reference round jet under the same conditions. He found out that in contrast to the round nozzle where the flow motion is dominated by large primary Kelvin-Helmholtz rings, for six-lobed rectangular jet secondary vortexes generated at the tip appear to be predominant, giving way to an incremented volumetric flow rate.

El Hassan [14]studied vortex structures for daisy-shaped orifice jets. He also found a higher entrainment for the daisy shape as related to circular jets. The reason for this is the generation of large-scale vortexes, which generated by the lobed geometry. In a similar way, El Hassan [15] also studied the effect of having a cross-shaped orifice.

Trávníček [30] studied the effect of implementing a system of synthetic jets distributed around the circumference of a primary nozzle. He found that excitation led to heat transfer increase in the stagnation area.

Cafiero [8] proved that implementing a fractal grid (a grid with a spare pattern repeated at increasingly smaller scales) enhanced the degree of turbulence at a slightly larger pressure drop. This way, it was possible to provide a significant heat transfer enhancement for relatively small nozzle-to-plate distances.

There have been initiatives on studying the effect of forcing pulsating impulses to the jet flow. Among them, Xu [34] performed a numerical study on this area and concluded that pulsations significantly increase the heat transfer for both cooling

and heating cases.

1.3 Purpose of this work

With some examples, it has been shown that strong efforts have been undertaken to understand how is turbulence related to heat transfer and the way to profit from it. Recent papers, like the one from Vinze [31] implemented different chevron configurations at the end of the flow pipes and observed an increase in the local Nusselt number on the plate. Vinze's work changes the number of chevrons, length and penetration depth.

Knowing that chevrons induce azimuthal vorticity to the flow, helping mixing and entrainment to take place, the purpose of this work is to evaluate the convective heat flux for different chevron configurations (for different chevron lengths, chevron numbers and chevron shape) for certain experimental conditions (Reynolds number and nozzle to plate distance). Temperature measurements are going to be taken with an infrared camera by making use of heat flux sensor and radiation theory. For that a pneumatic installation has to be mounted and knowledge in infrared measurement has to be acquired.

1.4 Project planning

For this project, the following steps were planned.

- **Gather information:** An introduction to the topic of heat transfer, impinging jets and infrared imaging had to be made. In order to perform the following steps involving design and apparatus set up, a good understanding of the physics of the problem and tools to be used had to be acquired. In order to reinforce the knowledge on impinging jets and help visualize the theory, simulations making use of COMSOL Multiphysics software were carried out.
- **Design of nozzle and nozzle caps:** Design work had to be performed in order to obtain chevron nozzle caps for the study. CAD software was used during this design and the pieces were 3D printed at the university.

- **Components selection and purchasing:** For this project, a pneumatic installation which had been previously mounted at the Propulsion Systems Laboratory of the university has been used. Still, some improvements and corrections had to be made in order to adapt the system to the desired operating conditions. Such changes involved for example, purchasing a new massflow meter for the appliance, as well as a set of tubes and fittings to adapt it to the system.
- **Installation assembly:** Once the components were bought, it was necessary to implement them for their use. At this point, special care was taken in order to obtain the proper connections, distances and angles for a better data acquisition.
- **Data acquisition process:** Measurements were performed and data were obtained for analysis. During this process, it has been checked that the results seemed consistent and useful for further modification in the installation.
- **Data post processing and analysis:** Making use of computational software, post processing lead to results, which had to be compared with literature for validation.

Chapter 2

Impinging Jets

For the purpose of this project and for a deeper understanding of the physics of the problem, it will be of interest to introduce some basics on impinging jets, the variables that have to be taken into account and an overview of its effects over a flat surface.

Although impinging jets can be found isolated or forming an array of jets, in this work only the single nozzle arrangement is investigated. In order to help visualize the explanation, some simulation results are going to be displayed. The software used for these simulations is COMSOL Multiphysics. For the simulations, one of the cases of study was taken: a simple round nozzle, two diameters away from the plate and with a Reynolds number of 10000. The radius of the nozzle is 7.5 mm and the outlet flow velocity is 10.33 m/s.

The Reynolds number is a dimensionless number and is defined as the ratios of inertial to viscous forces within a fluid subjected to relative internal movement due to different fluid velocities. For the case of jet flows, where the nozzle diameter D is taken as the reference length, the Reynolds number is given by Equantion 2-1

$$Re = \frac{\rho_f V \cdot D}{\mu} \tag{2-1}$$

whereρ is the fluid density, V is the jet flow velocity and μ is the dynamicic viscosity of the fluid. This non-dimensional parameter helps to predict the flow patterns under different flow conditions, determining for example the laminar to

turbulent transition.

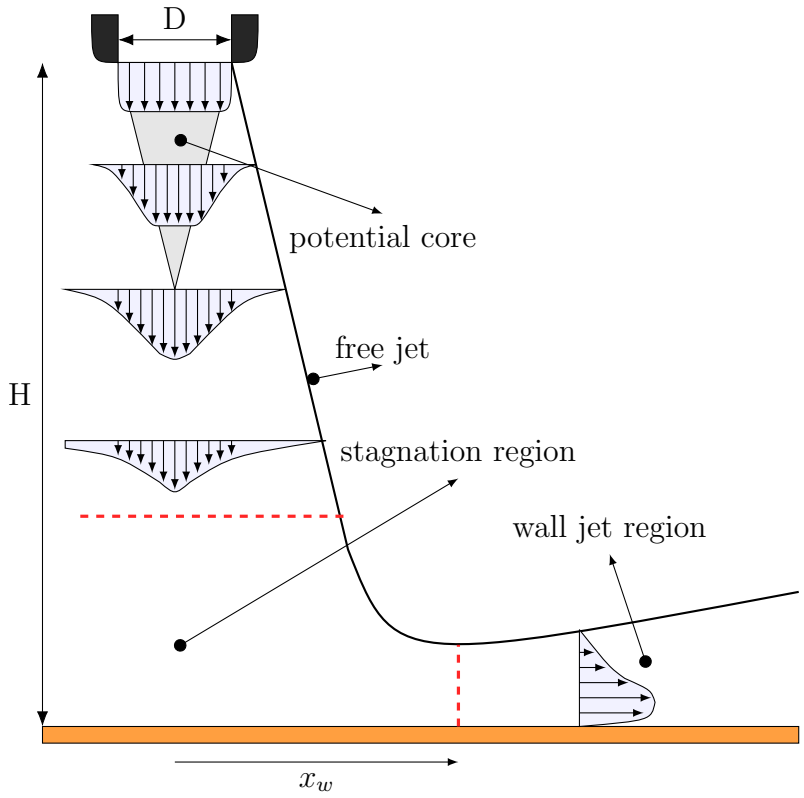

Figure 2-1: Sketch of an impinging jet.

An impinging jet is schematically displayed in Figure **2-1** and can be understood as a source of gas discharged from a nozzle onto a surface. Although later on, the object of interest will be impinging jets with chevron nozzles, for now the reader must think on a circular nozzle with exit diameter D at a distance H of the plate. In agreement to other studies on impinging jets, this nozzle to plate distance will be non-dimensionalized with the diameter of the nozzle exit (H/D).

Martin [22] describes the flow pattern of impinging jets as the ensemble of three regions: *free jet region* where the flow is not being perturbed by the impingement on the plate, a *stagnation region* where the flow is axially decelerated because of the effect of the impingement on the plate while accelerated in the radial direction, and a *wall jet region* where the flow velocity components are just parallel to the wall and behaves according to a wall jet rather than wall flow.

The jet develops starting from a turbulent state with a uniform velocity profile at the nozzle exit and as it travels away from the orifice, it experiences a momentum

exchange with the ambient. This momentum exchange causes the jet to widen while the *potential core* contracts, see Figure **2-2** . This potential core region is where the original flow velocity and total pressure are retained [10]. This way, the velocity profile of the jet leaving the nozzle reshapes from an almost rectangular contour spreading to the free boundaries and acquiring a Gausian-shape. See Figure **2-3**. In Figure **2-2** is is also seen how this momentum exchange traduces into some *flow entrainment* from the quiescent surrounding fluid.

For the problem of impingement cooling, this entrainment will be of special interest because it will effectively increase the volumetric mass flow impinging the surface. On the other hand, for better heat transfer at the stagnation region it will be important that potential core conditions are conserved as well. It has been found (and it will be seen in the results) that the optimal nozzle to plate distance for this is of 6 nozzle diameters.

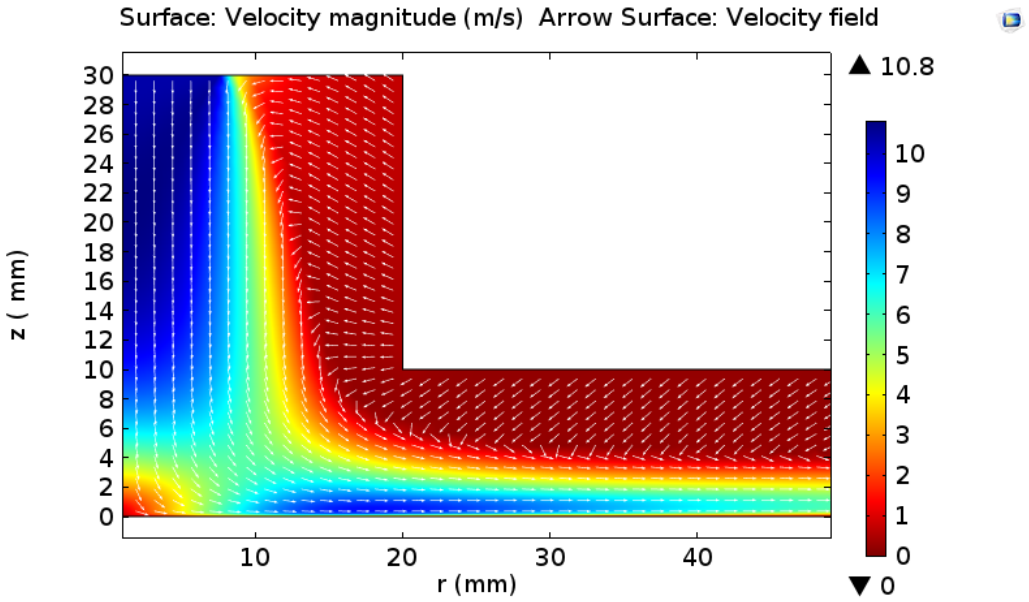

Figure 2-2: Absolute velocity magnitude distribution for the impinging jet flow and arrow field. Extracted from simulation Re 10000 and H/D = 2.

For the heat transfer over the solid surface, it will be of of special importance to understand what happens in the vicinity of the hot wall, since the flow velocity, size/behavior of the boundary layer and turbulence will be determining the heat transfer. As stated before, after reaching the stagnation region, the air will start to radially accelerate, up to point x_s (usually at around 4 nozzle radii according to [1]). The effect of acceleration keeps the boundary layer laminar in

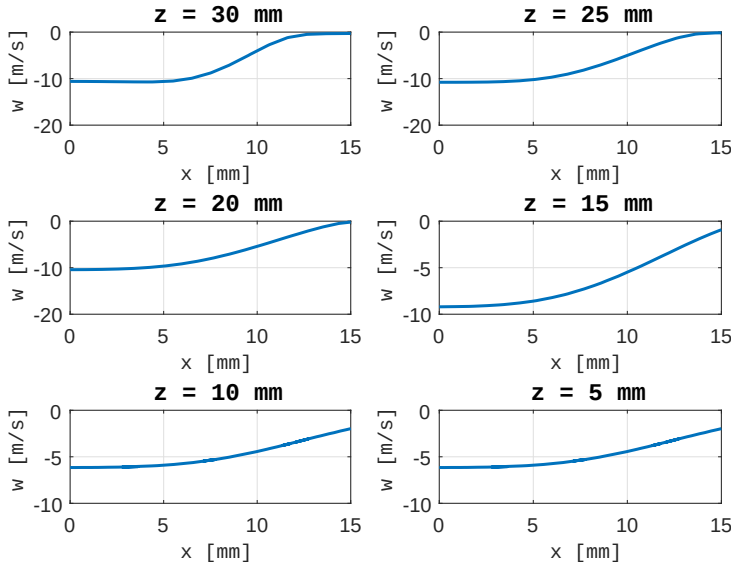

Figure 2-3: Axial velocity profiles from the axis symmetry axis at different distances from the impinged surface.

the stagnation zone, while in the contrary, after this maximum velocity point, a transition to turbulence takes place. From this point on, because both the velocity gradient at the wall and the gradient with the outside quiescent fluid, the boundary layer starts to grow and a wall jet appears. In Figure **2-4** a field for this radial velocities is displayed and the acceleration region is easily identified. In Figure **2-5**, radial velocity profiles for different radii are displayed. For x = 5 mm (right after the stagnation region), the flow is being accelerated. In the following two images, the wall jet can be good appreciated and for the image corresponding to x = 45 mm, far away from the maximum radial velocity and already well into the turbulent regime, the wall jet has disappeared. It is also recognized that as the boundary layer develops, the point of maximum velocity in the profile finds itself further up from the wall and this locus of maxima will lead to the boundary layer thickness distribution, according to Martin [22].

In the turbulent region, the magnitude of the maximum velocity of the jet will be decaying to zero as the flow goes on (Figure **2-6**).

The *nozzle-to-plate distance* (H/D) plays a crucial role in the development of this potential core which directly affects the magnitude and distribution of the local heat transfer coefficients over the impinged surface. In Figure **2-7** this phenomenon is easily identified. For an impinged surface, knowing that the local heat transfer properties of a circular jet will have an axisymmetric distribution,

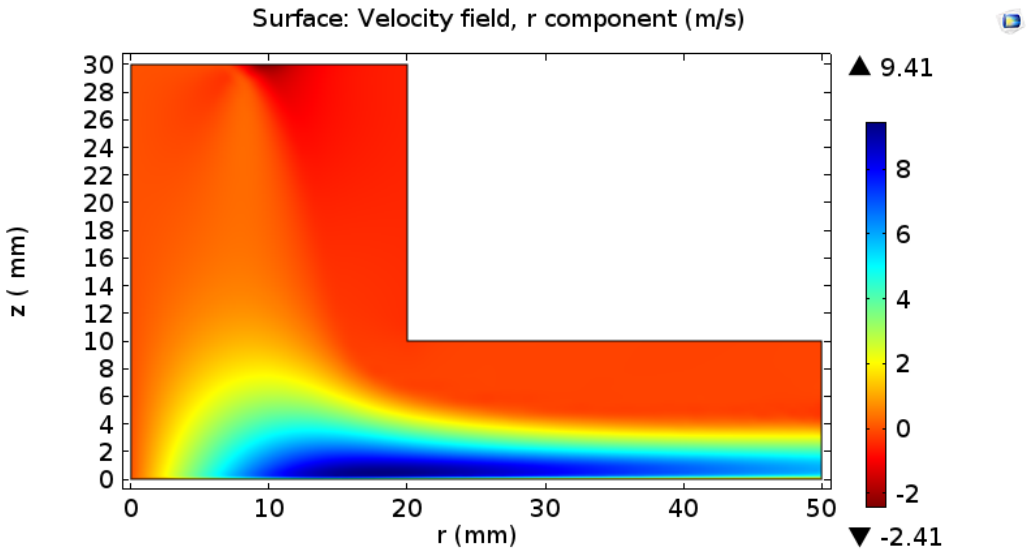

Figure 2-4: Radial velocity field.

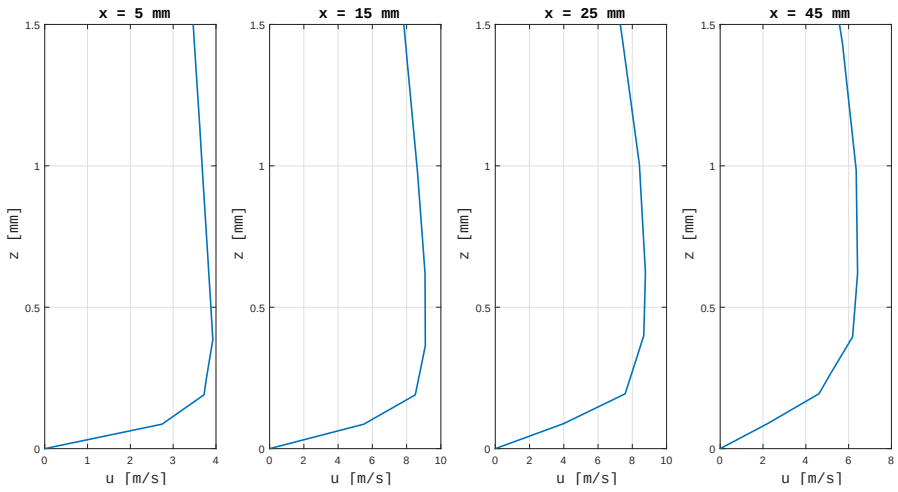

Figure 2-5: Radial velocity profiles for at different distances from the stagnation point.

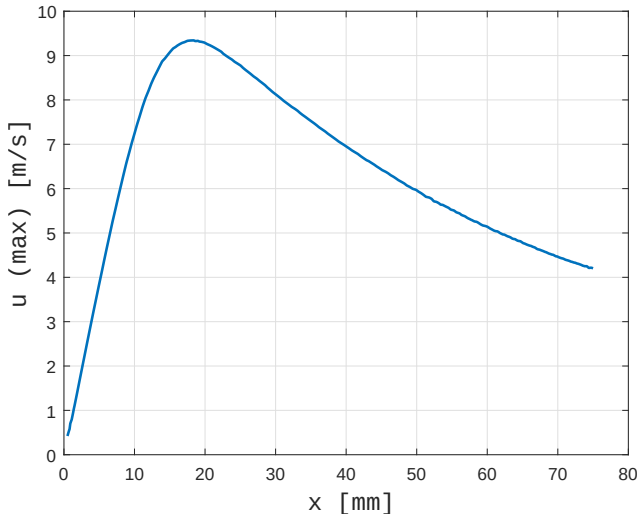

Figure 2-6: Maxima in the radial velocity for different distances from the stagnation point.

they can be plotted as an only function of the radial distance to the stagnation point r/D.

For large distances, it is seen that the maximum heat transfer coefficient is found at the stagnation point and it will be radially decreasing in a bell-shape. For nozzle-to-plate distances $H/D < 6$, the central peak is replaced by a heat transfer minimum surrounded by an annular peak (*inner peak*). As H/D continues decreasing, an annular hump starts to develop around this inner peak and grows till at a nozzle-to-plate distance of 3, it appears a well defined secondary annular peak (*outer peak*). The appearance of the second maximum is attributed to a sharp rise in the turbulence level which accompanies the transition from an accelerated stagnation region flow to a decelerating wall jet [22]. Indeed, comparing Figures **2-7** and **2-6**, one can see that the location of the outer annular peak is pretty close to the point of maximum radial velocity and right before transition to turbulence.

Given that the impinging jets is a good way to enhance heat transfer, there have been a lot of research initiatives to manipulate and optimize the value and location of these heat transfer coefficient maxima. For that, tests have been made varying nozzle to plate distances, Reynolds number of the flow and adding elements to the nozzle exit as it is the case of the chevron nozzle, nozzle chamfering and the implementation of confined nozzles. Examples of these studies can be found at papers from Violato [32], Ianiro [10] and Choo [12].

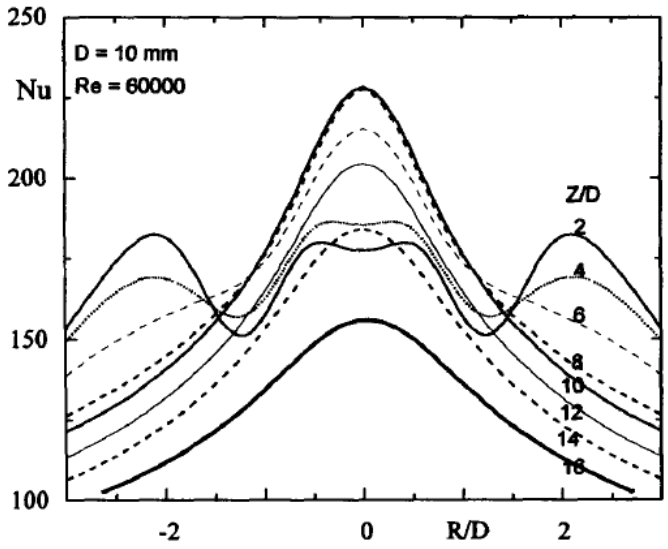

Figure 2-7: Nusselt number radial distributions for various nozzle-to-plate distances [23].

It is worthy to note that if the nozzle is placed closer than a half nozzle diameter, the impingement of the jet is substituted by a wall jet with relatively high heat transfer rates.

2.1 Introduction to chevron nozzles

In this project, the object of study is the heat transfer performance of different chevron nozzles, although their first application was not in the field of impingement heat transfer. The idea of adding chevrons at the the rim of nozzles came from the necessity of reducing jet noise and infrared signature of the aircraft engines [6]. Jet noise is primarily produced by shear effects between the jet and ambient flow. Reducing the exhaust jet velocity and promoting mixing of jet and ambient flow is a good way to reduce jet noise, but this is difficult to be achieved without compromising the engine performance.

Here is where the practice of adding chevrons to the nozzle rim comes into play, so they generate axial vorticity encouraging the jet air to mix faster with the surrounding fluid. In year 1999, GE started a program to develop a noise reduction upgrade to the CFM56-5B [21] and nowadays chevrons are seen for example in the engines of B747 airplanes. See Figure **2-8**.

Figure 2-8: B747 exhaust nozzles.

Later on, it was seen that the effect of adding chevrons to nozzles can be used to heat transfer enhancement for industrial applications. So it was known that the fundamental physical process at the origin of heat transfer is associated with the flow turbulence and its three-dimensional behavior in the region of impingement [32]. If the flow reaches the impingement surface with a higher degree of turbulence, a higher heat transfer rate will be achieved.

2.2 Parameters and geometry of chevron nozzles.

In the line of reducing noise making use of chevron nozzles, Bridges and Brown [7] presented a paper in year 2014 describing the relationship between chevron geometric parameters, flow characteristics and far-field noise. As stated before, it will be of special interest a good turbulent mixing although the effective jet velocity sees itself reduced.

Implementation of chevrons induces axial vorticity in the flow, which increases cross-stream trasport and mixing in the shear layer of the potential core. Because closely spaced chevrons generate vortexes that tend to annihilate one each other and limit the cross-stream transport they should accomplish, it will be of interest to manage an optimal axial vorticity distribution within the cortex core. For this end, the main flow field parameters to vary are *vortex strength*, *vortex spacing*

and *vorticity distribution*. These parameters are related to the following geometry variables: *chevron penetration*, *chevron count* and *chevron length* respectively. Combining these variables Bridges and Brown were able to vary the *effective nozzle diameter* and define a *vortex strength parameter*.

In Figure **2-9**, chevron length and penetration are displayed.

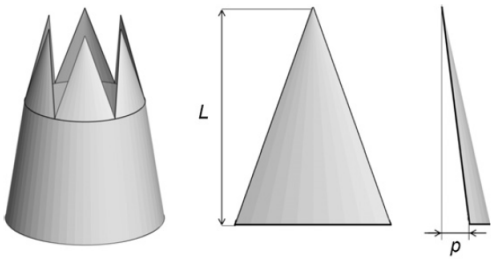

Figure 2-9: Details of the chevron geometry: length L and penetration depth p. [32]

2.3 Jet development and differences between round and chevron nozzles.

Violato and Scarano [32] [33] made a deep study of the development of circular jet flow and compared it to the jets product of chevron nozzles.

For the circular impinging jet and moderate Reynolds numbers, in the region close to the nozzle rim, Kelvin-Helmholtz instabilities (azimuthally coherent) originate and will later on be organized in toroidal vortexes (or vortex rings). These donut shape vortexes will pair downstream. During this vortex pairing, streamwise instabilities are formed and also radial vorticity coherence is seen to grow. Instead of toroidal vortexes, the chevron jet develops in a star-shaped pattern with regions of higher axial and radial velocity components in correspondence to the chevron notches. See Figure **2-10** and **2-11**.

2.3.1 Heat transfer

It is interesting to check at the differences in pattern and values that the heat transfer coefficients acquire over the impinged surface. The paper of Violato

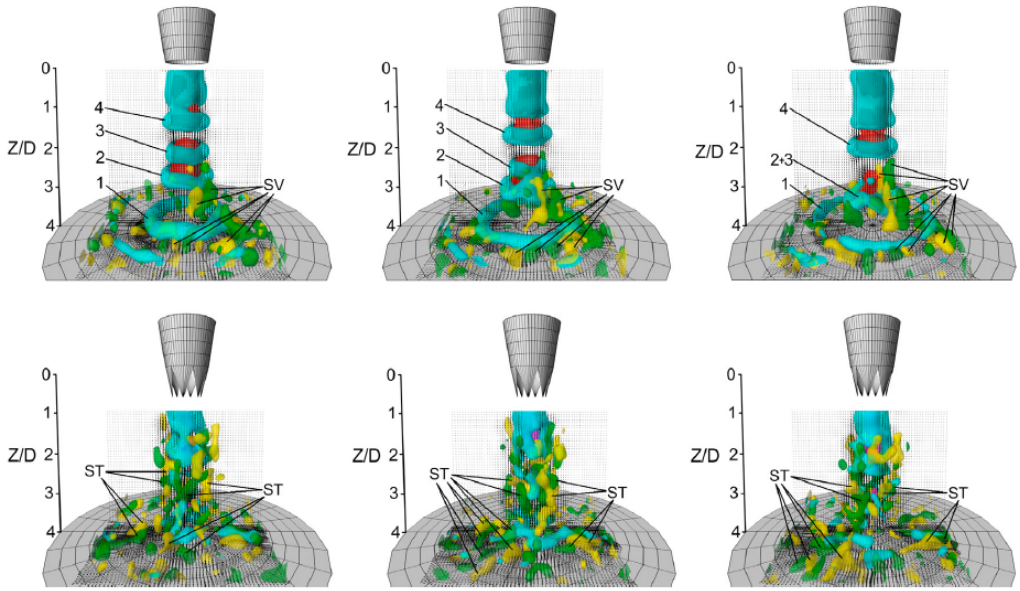

Figure 2-10: Temporal sequence of instantaneous iso-surface axial velocity $W/W_j = 1.45$ (red in the circular jet) and 1.7 (purple in the chevron jet), azimuthal vorticity $\omega_\theta D_j/W_i = 4$ (cyan), axial vorticity $\omega_z D/Wj = -1.2$ (green) and 1.2 (yellow). Vectors on plane $Y/d = 0$. Time separation between snapshots $\Delta t W_j/D = 0.45$. [32].

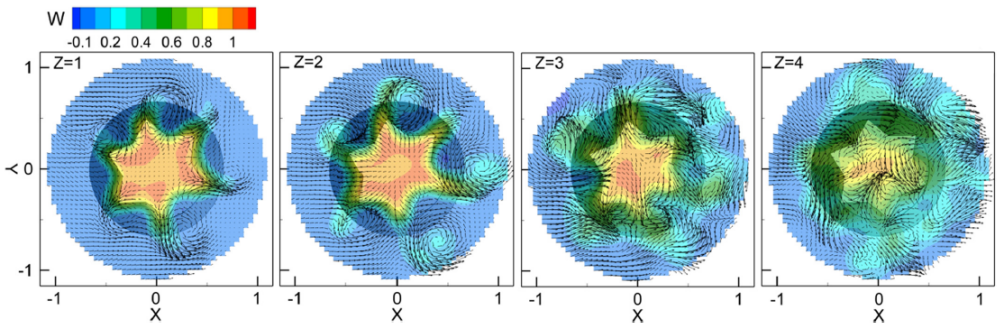

Figure 2-11: Chevron jet: contours of mean-axial velocity at different cross-sectional Z-planes; X-Y projection of velocity vectors. [33].

[32] elaborates a good description of this heat transfer coefficients distribution and some of his results are going to be used to validate the outcomes of this experiment.

In Violato's Nuselt maps and for the case of circular nozzle jet the two axisymetric maxima stated before are clearly seen and for the case of a chevron nozzle, a star-shape in concordance to the chevron distribution appears. In the center higher Nusselt number values than for the circular case are observed, as well as in the star segments corresponding to the nozzle notches.

Chapter 3

Heat Flux Sensors

For this experiment, it will be necessary to accurately measure the local *convective heat flux*, $q_{conv}[W/m^2]$, making use of infrared thermography technique. For that it will be necessary to calculate the *convective heat transfer coefficient* $h[W/m^2K]$. The relationship between these two terms is given by the Newton's convection law

$$q_{conv} = h(T_w - T_{jet}) \tag{3-1}$$

where T_w is the surface temperature of the wall and T_{jet} is the jet temperature, which in principle in approximate to the ambient temperature. For the calculations, in order to remove the dependence on the ambient temperature, a temperature T_{cold} (the temperature of the system without energy contribution) and a temperature T_{hot} (the temperature of the system after applying Joule heating) is going to be taken. Transforming Equation 3-1 into Equation 3-2.

$$q_{conv} = h(T_{hot} - T_{cold}) \tag{3-2}$$

Data is generally presented in terms of the *Nusselt number*

$$Nu = \frac{hL}{k_f} \tag{3-3}$$

Here, L is a characteristic length (for the Nusselt number calculation, nozzle

diameter will be taken) and k_f is the thermal conductivity of the fluid.

Heat flux sensors generally consist of a plate with well known thermal properties and whose energy will be measured by the infrared camera. Knowing the properties of the flow and the temperature differences, one can apply an energy balance to develop a suitable thermal model to calculate the desired thermal parameters.

Before proceeding, it is necessary to point out the names given to the slab surface in contact with the flow (*front surface*) and the opposite one (*back surface*). It will be also necessary to introduce the *Biot number* (Bi), a parameter used to evaluate the thermal thickness of a slab.

$$Bi = \frac{h_t s}{k_{plate}} \tag{3-4}$$

In this relationship, h_t is the total heat transfer coefficient that includes convection and radiation, s is the slab thickness and k_{plate} is the thermal conductivity of the sensor.

For IR thermography, three classical heat flux sensors are commonly used [3]:

- *Heated thin foil sensor*: This sensor normally consists of a thermally thin ($Bi << 1$) metallic sheet or a printed circuit board, which is steady and uniformly heated by Joule effect. Taking advantage of Joule effect and the relative high conductivity of the material, one can make sure this uniformity condition.
- *Thin film sensor*: This time, a thermally thick slab is used as a sensor instead, and the convective heat transfer coefficient is deduced from the unsteady heat conduction in a semi-infinie solid.
- *Thin skin* or *wall calorimeter*: For this sensor, a thermally thin slab is used as a perfect calorimeter. In order to do that, the time rate of temperature change is evaluated and modeled.

It is important to note that, according to Astarita [2], the most typically used heat-flux sensors are the ones known as *one-dimensional*. For these sensors, the heat flux to be measured is assumed to be transverse to the sensing surface. A first approximation considering one dimensional sensor can be estimated (denoted as the *ideal* case), but then an extension to the multi-dimensional configuration

needs to be made, since for real applications, effects of lateral conduction and transient convection need to be taken into account for a proper data processing.

For the purpose of this work, it is relevant to focus on the heated thin foil sensor.

3.1 Heated Thin Foil Sensor

The convective heat transfer coefficient can be quantified by measuring the heat input as well as the foil surface temperature with the infrared scanner.

The ambient temperature T_a is assumed to be constant, so the ambient environment can be considered as a black body (what a black body is will be explained in Chapter 4).

According to the diagram in Figure **3-1**, one needs to account for the radiative heat leaving the surface of the sensor q_{rad}, the convection contribution q_{conv}, an other contribution due to thermal conduction across the foil q_{cond} and a last term accounting for the natural convection q_n on the back surface of the heated thin foil sensor.

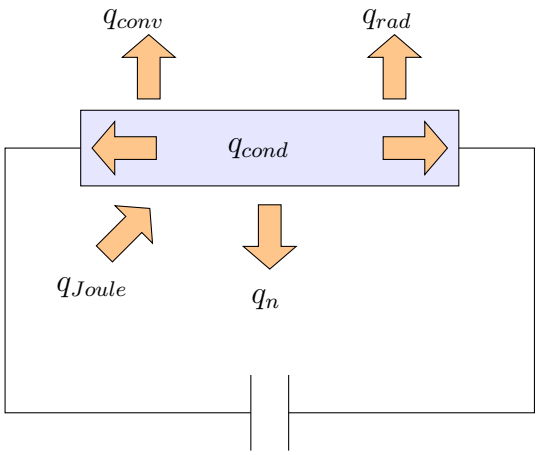

Figure 3-1: Sketch of heated thin foil sensor. Diabatic back surface.

Conservation of energy for the case of the heated thin foil sensor, without taking into account the unsteady term, results to be:

$$q_{Joule} = q_{rad} + q_n + q_{conv} + q_{cond} \tag{3-5}$$

At this point it is interesting to introduce the expressions of the terms in Equation 3-5. So, from here on one can extract the convective heat transfer coefficient, h. This value will be used in order to calculate the Nusselt number, either for one point or like in this case, a Nusselt number distribution.

$$q_{Joule} = \frac{VI}{A} \tag{3-6}$$

$$q_{rad} = \epsilon\sigma(T_w^4 - T_\infty^4) \tag{3-7}$$

In these equations V is the voltage supplied, I the corresponding current intensity, A is the area of the heated foil sensor, ϵ is the emissivity of the material, σ the Stefan-Boltzmann constant, T_w the wall temperature and T_∞ the temperature far away from the surface. The temperatures are in Kelvin.

A phenomenon like the one of study, implies that the heat transfer coefficient varies. So does the sensor surface temperature. Consequently temperature gradients force heat fluxes in the tangential directions, but by the assumption that the sensor is thermally thin and ideal, this can be easily modeled by means of Fourier law:

$$q_{cond} = -k_{plate} s \nabla^2 T_w \tag{3-8}$$

By neglecting natural convection q_n, after equating Equation 3-5 and solving Equation 3-3 for h, the final expression for the convective heat transfer coefficient will be

$$h = \frac{q_{Joule} - q_{rad} - q_{cond}}{T_{hot} - T_{cold}} \tag{3-9}$$

3.1.1 Natural Convection contribution

The natural convection phenomenon is the result of body forces such as gravity acting on a fluid in which there are density gradients. This natural convection is also known as free convection because there is no instrument forcing the fluid to move. Because the velocity of this fluid is much lower than in the forced case, the heat transfer coefficient is also quite low.

There are several cases of study for the determination of the relevance of free convection, depending on the orientation of the plate and on the temperature difference between the plate, T_s and the ambient, T_∞. It is of interest the case of the natural convection under a horizontal hot plate, refer to Figure **3-2**.

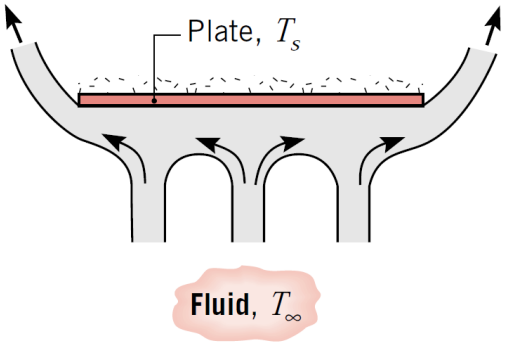

Figure 3-2: Buoyancy-driven flow over the bottom surface of a hot horizontal plate [5]

Here, the tendency of the fluid to ascend is impeded by the plate. The flow must horizontally displace before it can ascend from the edges of the plate [5].

For this situation

$$\overline{Nu_L} = 0.27 Ra_L^{1/4} \tag{3-10}$$

where

$$Ra_L = \frac{\rho g \beta (T_s - T_\infty) L^3}{\mu \alpha_d} \tag{3-11}$$

In this Equation 3-11, g is the gravity constant, β is the volumetric thermal expansion coefficient, which for an ideal gas is

$$\beta = \frac{1}{T} \tag{3-12}$$

bein the temperature in absolute value. T_s is the surface temperature, T_∞ the ambient temperature, ρ the fluid density, L a characteristic length, μ the dynamic viscosity and α_d is the thermal diffusivit of the fluid under the determined temperature and pressure conditions. These values are taken from the tables of Thermophisical Properties of Gases at Atmospheric Pressure [5].

Noting that for this case the characteristic length is given by

$$L = \frac{plate\, surface}{plate\, perimeter}$$

the Nusselt number value for the natural convection of the plate is around 7.3, which is quite low in comparison with the forced convection Nusselt numbers resulting from the impinging of the jet shown in the next sections. . For this reason, natural convection will not be taken into account.

3.1.2 The printed circuit board.

For the development of these experiments it was decided to implement a printed circuit board as a heated-thin-foil sensor. Several adjacent thin copper tracks are printed and arranged in a Greek fret mode and bound to a fiberglass substrate. Because of the high conductivity of copper, the board shows an anisotropic thermal conduction behavior (different in each direction) and for this reason instead of making use of Fourier law as in the case of a thin foil, the conduction term has to be expanded to

$$q_{cond}(x,y) = -\underline{\nabla}(s(x,y)\underline{\underline{\Lambda}}(x,y)\underline{\nabla}T_w(x,y)) \tag{3-13}$$

By choosing a cartesian coordinate system with axes directed as the two principal axes of the thermal conductive tensor $\underline{\underline{\Lambda}}$, it is possible to split this effect in the directions parallel and normal to the copper tracks, obtaining

$$q_{cond} = q_{cond,x} + q_{cond,y} \tag{3-14}$$

Figure **3-3** serves as an illustration for the problem.

In Equation 3-14, $q_{cond,y}$ happens to be the addition of two conduction mechanisms: the heat flux due to the copper tracks and due to the fiberglass support.

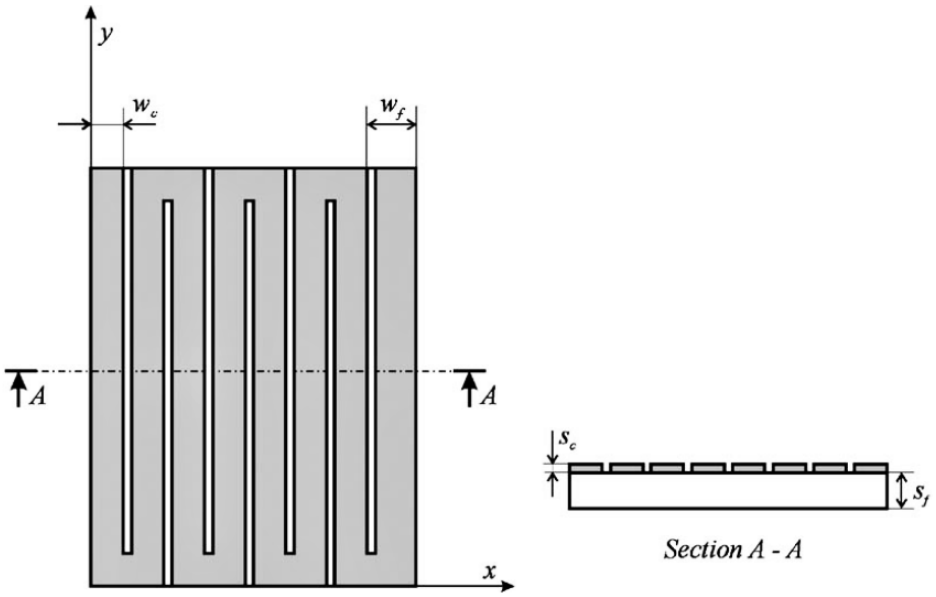

Figure 3-3: Printed circuit. [2]

$$\begin{aligned} q_{cond,y} &= -\Big(\frac{w_c s_c \lambda_c + w_f s_f \lambda_f}{w_f}\Big)\frac{\partial^2 T_w}{\partial y^2} \\ &= -(\gamma^* s_c \lambda_c + s_f \lambda_f)\frac{\partial^2 T_w}{\partial y^2} = -(s\lambda)_{ey}\frac{\partial^2 T_w}{\partial y^2} \end{aligned} \tag{3-15}$$

Here w indicates the width, s the thickness, subscripts c and f correspond to copper and fiberglass. λ_f and λ_c are the thermal conductivity coefficients of the copper and fiberglass respectively. A width parameter γ^* was implemented to simplify the expression.

$$\gamma^* = \frac{w_c}{w_f} \tag{3-16}$$

$(s\gamma)_{ey}$ stands for equivalent thermal conductance along the y-axis.

When looking at the x-direction, the one perpendicular to the copper tracks, in the gap zone only fiberglass allows conductive heat transfer while, in the track zone, both copper and fiberglass contribute to it. So, the heat flux in this direction will be formulated as

$$q_{cond,x} = -\Big(\frac{1-\gamma^*}{s_f\lambda_f} + \frac{\gamma^*}{s_c\lambda_c + s_f\lambda_f}\Big)^{-1}\frac{\partial^2 T_w}{\partial x^2} = -(s\lambda)_{ex}\frac{\partial^2 T_w}{\partial x^2} \tag{3-17}$$

where $(s\lambda)_{ex}$ represents the equivalent conductance along the x-axis.

After applying this correction, one can go back to Equation 3-9, find the value of the local convective heat transfer coefficient and set it into Equation 3-3 to find the corresponding Nusselt number.

3.1.3 Remarks

In this set of equations the reader can see that most of the terms are either physical constants or properties of the material an geometry of the appliance. In the heated-foil-sensor used, the voltage for the Joule heating is an input and the only parameters that actually count for the h and Nu determination is the difference in temperature between the T_{cold} and T_{hot} conditions. T_{hot} is the temperature of the plate when then electric circuit is switched on, and T_{cold} is the temperature measure then the electric circuit is switched off.

Up to this point, the reader may notice too that in Equation 3-3, the thermal conductivity of the fluid needs to be implemented, but this parameter depends on the the fluid temperature above the surface which is neither the temperature of the free stream, nor the temperature of the hot plate. During the calculation an average temperature, called T_{film}, was taken.

Chapter 4

Radiation Theory and IR scanner

In contrast to other means of heat transfer like conduction or convection, when talking about radiation one has to have in mind that there is no need of a physical medium for it to happen. Radiation takes place in vacuum and its effect does not result negligible in industrial applications and energy conversion methods.

At this point it results important to have a deep understanding of this heat transfer phenomenon, since it is going to be the one that will allow the acquisition of data for the experiment. Furthermore, it will approach the reader to the understanding of the way the IR camera works.

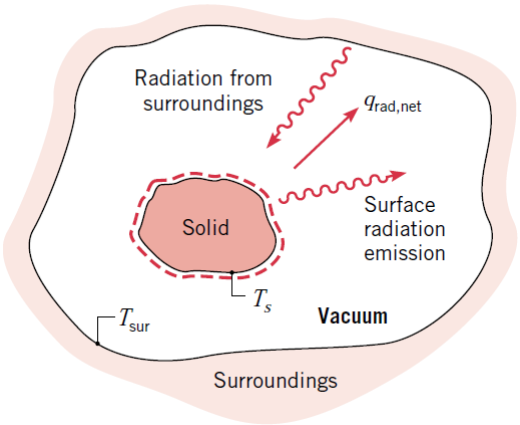

Figure 4-1: Radiation cooling of a heated solid [5].

For the study of this heat transfer phenomenon, the bodies will be considered in vacuum (still in presence of an atmosphere, one would only have to deal with it

applying the proper corrections). It is well known that thermal energy flows from bodies with a higher energy to bodies with lower one. The body will receive some energy in form of radiation from the surroundings and cool down while radiating free energy back to the surroundings. This cooling down is associated with a reduction of internal energy stored, which is released as a result of oscillations or transitions of the many electrons that constitute matter.

Radiation is a *volumetric phenomenon* because the heat emerging from a finite volume of matter (solid, liquid or gas) is the integrated effect of local emission through the volume. That means that the radiation emitted by the internal molecules of the volume to be considered, is strongly absorbed by the adjoining molecules and at the end, only the energy actually coming out of the control volume will be to be considered. For this reason, it is useful sometimes to concentrate in situations for which radiation is a *surface phenomenon*. It has been observed, that the radiation emitted from a solid or a liquid originates from molecules that are within a distance of approximately 1 μm from the exposed surface.

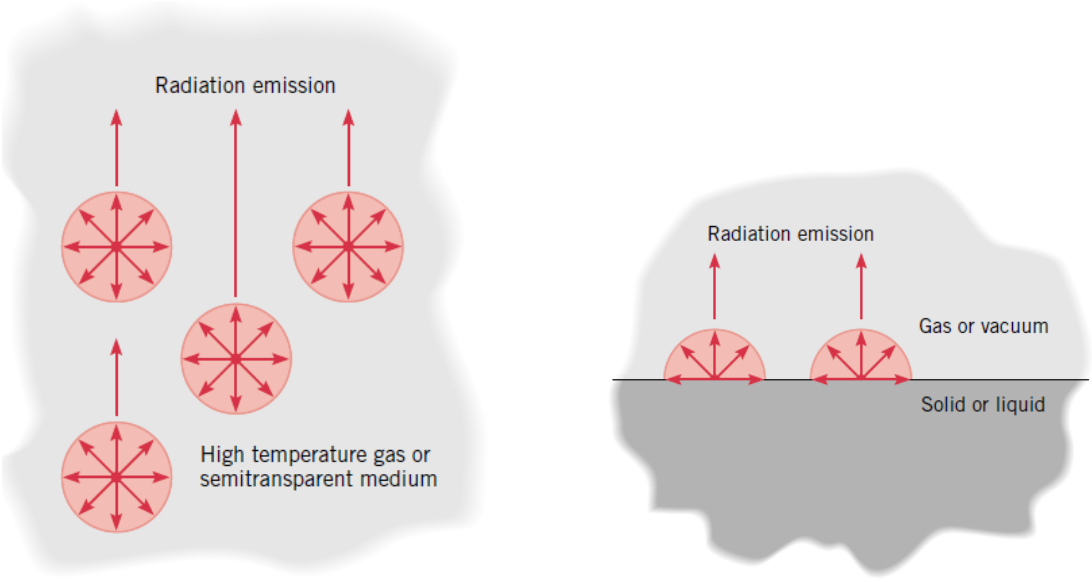

(a) As a volumetric phenomenon. (b) As a surface phenpmenon.

Figure 4-2: Emission process [5].

Answering the question of what is actually the mean of propagation of energy of a radiating body, one can describe it as the fact that just because of being at a temperature above the absolute zero, the movement of charged particles results in the emission of electromagnetic waves traveling in vacuum. The characteristics

of these waves depend on several variables, such as the material of the radiating body and its surface finish, the thermodynamic state and its specific wave length, which is described as

$$\lambda = \frac{c_o}{\nu} \tag{4-1}$$

For infrared thermography applications, it will be useful to consider this value in terms of μm. c_o is the speed of light in vacuum, which takes the value of $c_o = 2.998 \cdot 10^8 m/s$ and ν is the frequecy of the wave and will be expressed in term of s^{-1}.

The speed of light and the wave length will depend on the nature of the medium and the frequency will depend only on the source of the electromagnetic wave. This fact is directly related to another way of approaching the quantification of radiation, which is based on quantum theory. At this point, radiation will be seen as a collection of discrete particles termed photons whose energy will be defined as

$$e = \hbar\nu = \hbar\frac{c_o}{\lambda} \tag{4-2}$$

This energy e is expresed in Joules and the Plank's constant takes the value $\hbar = 6.626 \cdot 10^{-34} Js$. Knowing that the magnitude of radiation varies with wave length, it is possible to describe an electromagnetic spectrum of it and notice that thermal radiation (the one of interest for the thermography scanning to be performed in this experiment) encompasses just a discrete range of wave lengths.

This thermal radiation band is relatively small and ranges from 0.1 μm to 100 μm. In particular, when a body is at ambient temperature most of the energy is radiated in the infrared spectral band. This band is at the same time, sub-divided into four smaller bands called: *near infrared* [0.76 - 3 μm], *middle infrared* [3 - 6 μm], *long infrared* [6 - 15 μm] and *extreme infrared* [15 - 100 μm]. For the IR thermography application, most of the sensors are sensitive to the middle (MWIR) or the long wavelength (LWIR) spectral bands.

There are two remaining features that describe radiation. On the one side, it is to take into account the *spectral distribution* radiation describes. This is related to the temperature and the nature of the emitting surface. The second feature is known as *directionality*, which as seen in Figure **4-4**, denotes that a surface may

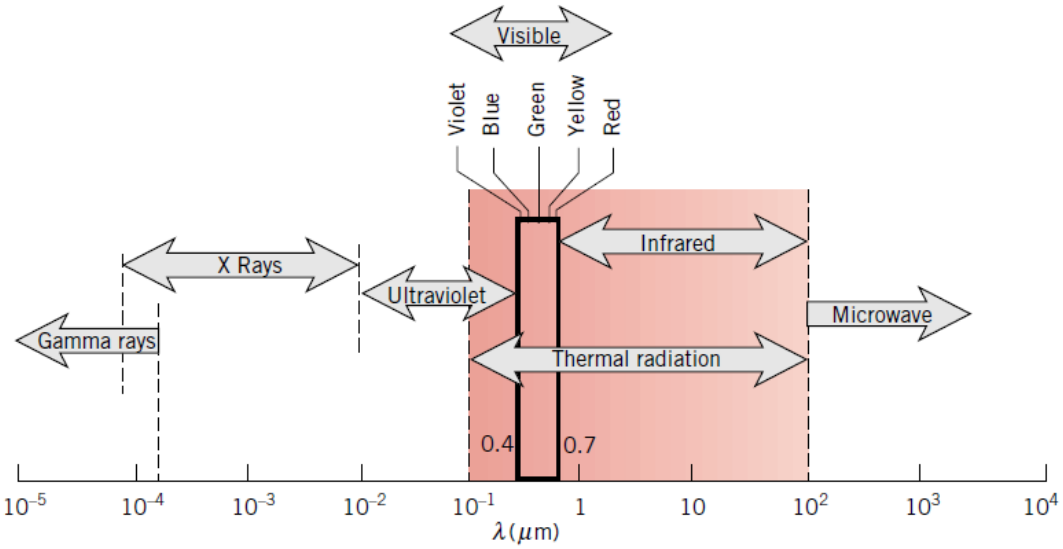

Figure 4-3: Spectrum of electromagnetic radiation [5].

emit preferentially in certain directions creating a *directional distribution* of the emitted radiation.

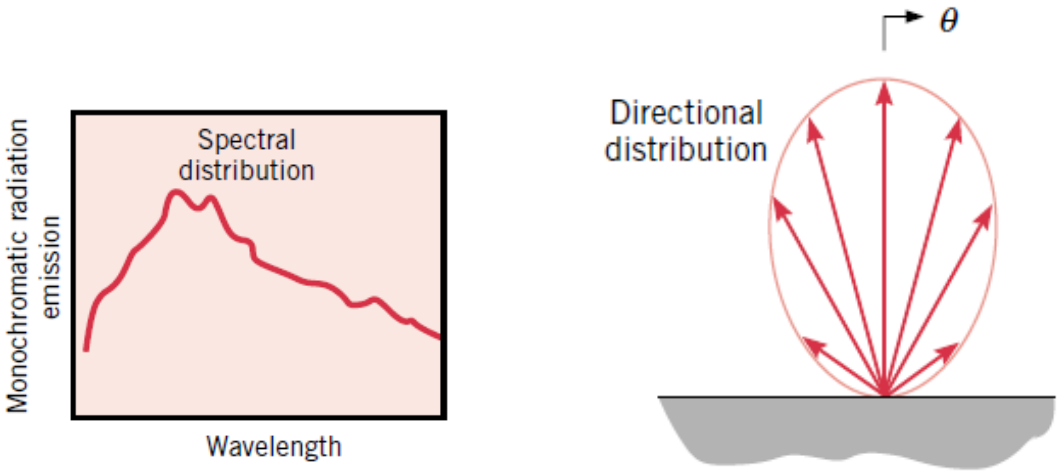

(a) Spectral distribution. (b) Directional distribution.

Figure 4-4: Radiation emitted by a surface [5].

4.1 Black Body Radiation

A *blackbody* is defined as a perfect emitter and absorber of radiation. Is the one that [5]:

1. Absorbs all incident radiation, regardless of wavelength and direction.
2. Emits the highest energy for a prescribed temperature and wavelength.
3. Emits radiation, which is independent of direction. In other words, it is a diffuse emitter.

It serves as a standard against which the radiative properties of actual surface may be compared.

To put an example, one can think in the case in which radiation enters a cavity whose inner surface is at uniform temperature as the one shown in Figure **4-5**. Here, the reader can see how all radiation enters the cavity without being reflected, while it is able to leave the cavity through a small orifice uniformly emitting in all directions.

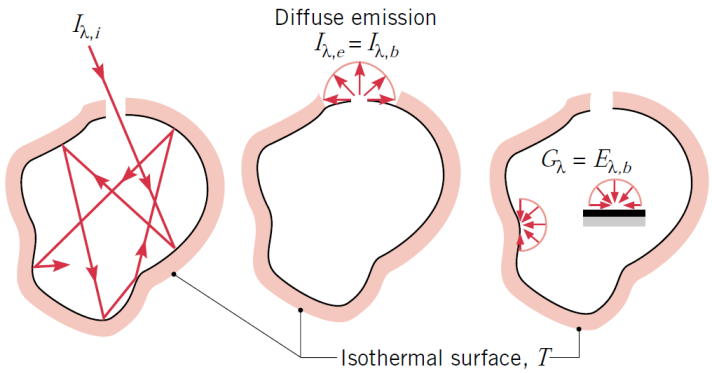

Figure 4-5: Characteristics of an isothermal blackbody cavity: Complete absorption, diffuse emission from an aperture and diffuse irradiation of interior surfaces [5].

The radiation energy emitted by a black body per unit time and per unit surface area is given by the experimental *Stefan-Boltzmann law*

$$E_b(T) = \sigma T^4 \tag{4-3}$$

where the *Stefan-Boltzmann* constant is $\sigma = 5.670 \cdot 10^{-8} W/m^2 \cdot K^4$ and the absolute temperature of the surface T will be given in Kelvin.

Stefan-Boltzmann law determines the total blackbody emissive power E_b, which happens to be the sum of radiation emitted over all wavelengths. In some cases,

it will be of interest to know the spectral blackbody emissive power which is the amount of radiation energy emitted by a blackbody at a thermodynamic temperature T per unit time, per unit surface area, and per unit wavelength about the wavelength λ [11].

The relation for the spectral black body emissive power is

$$E_{b\lambda}(\lambda, T) = \frac{C_1}{\lambda^5[exp(C_2/\lambda T) - 1]} \tag{4-4}$$

and is given in $W/m^2 \cdot \mu m$. Here $C_1 = 2\pi hc_o^2 = 3.74177 \cdot 10^8 W \cdot \mu m^4/m^2$ and $C_2 = hc_o/k = 1.43878 \cdot 10^4 \mu m \cdot K$.

At this point it is interesting to introduce the *emissivity* (ϵ) to the list of definitions. The emissivity is known as the ratio of radiation emitted by the surface at a given temperature to the radiation emitted by a blackbody at the same temperature. It varies in the interval [0, 1] and the black body adopts $\epsilon = 1$. The emissivity of materials will be later taken into account when focusing and calibrating the camera, as well as while designing a proper heat-flux sensor for the measurements.

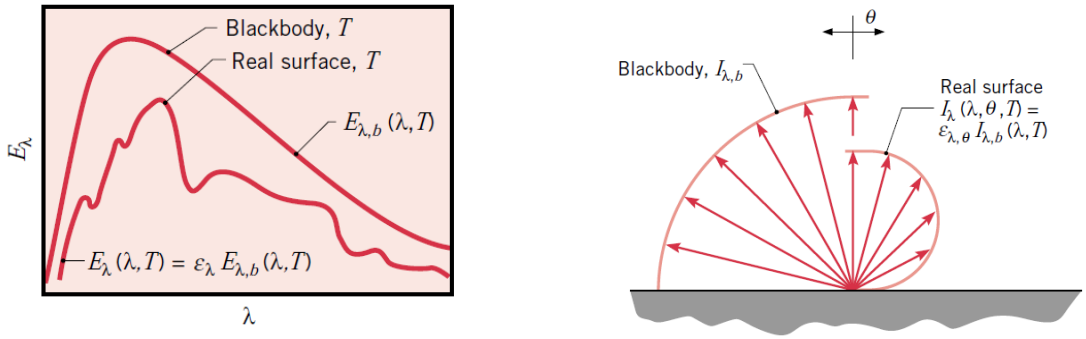

(a) Spectral distribution (b) Directional distribution

Figure 4-6: Comparison of blackbody and real surface emission [5].

In general, the spectral radiation emitted by a real surface disagrees from the Planck distribution for a real body. In addition, the directional distribution for the emission of a real body does not appear to be diffuse, like for a black body. Figure **4-6** schematizes this these differences.

Absorptivity	$\alpha = \frac{Absorbed\ radiation}{Incident\ radiation} = \frac{G_{abs}}{G}$	$0 \leq \alpha \leq 1$
Reflectivity	$\rho = \frac{Reflected\ radiation}{Incident\ radiation} = \frac{G_{ref}}{G}$	$0 \leq \rho \leq 1$
Transmissivity	$\tau = \frac{Transmitted\ radiation}{Incident\ radiation} = \frac{G_{tr}}{G}$	$0 \leq \tau \leq 1$

Table 4-1: Summary of radiative properties.

4.2 Other radiative Properties

- **Absorptivity** α**:** Fraction of irradiation absorbed by the surface.
- **Reflectivity** ρ**:** Ratio of irradiation absorbed by the surface.
- **Transmissivity** τ**:** Fraction of transmitted radiation through the medium.

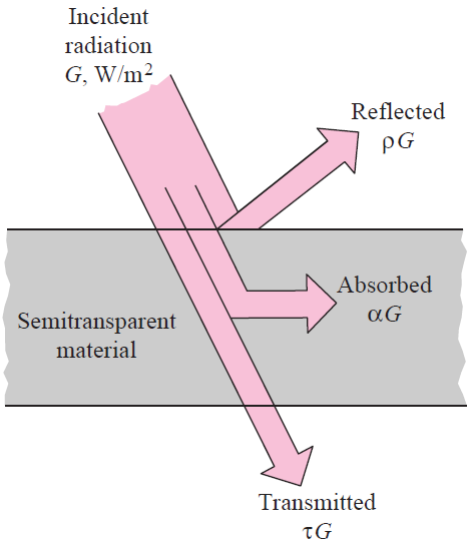

Figure 4-7: The absorption, reflection, and transmission of incident radiation by a semitransparent material. [11].

Being G the incident radiation, the radiative properties are defines as:

Adding terms, energy conservation requires:

$$G_{abs} + G_{ref} + G_{tr} = G \tag{4-5}$$

After normalizing Equation 4-5 transform into

$$\alpha + \rho + \tau = 1 \tag{4-6}$$

Again, the knowledge and understanding of these properties will be important for the calibration of the IR camera.

4.3 IR scanner

One of the most important elements during the performance of these experiments, will be the infrared camera, or IR scanner. This camera, the same way as an optical one, collects a radiative signal through an optical system and sends the information into a temperature detector that is sensitive to the selected radiation band. In this case the signal will be delimited into the infrared band. This temperature detector generates an electrical signal, which will be acquired by a video frame grabber and is later processed by an electronic board in order to obtain a temperature map of the scanned scene [9]. How this works is schematically shown in Figure **4-8**.

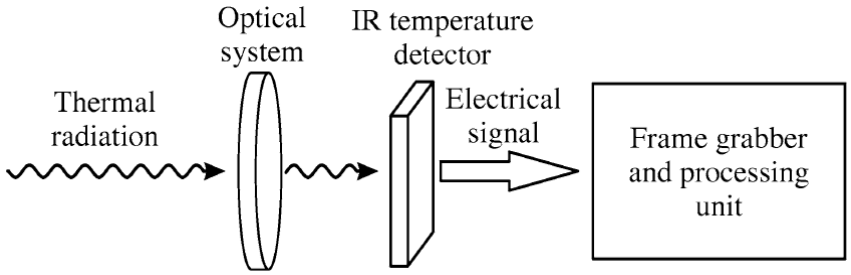

Figure 4-8: Essential components of an IR scanner. [3]

The available IR scanner is the FLIR SC4000 MWIR camera.

4.4 Optical System

The IR scanner optical system is composed by a lens, that the same way that for a photographic camera, has to be transparend in the used infrared band. Filters

could also be used to improve the performance of the scanner. In this case, no filter will be implemented.

4.5 IR Temperature Detector

Once the radiation has gone through the optical system, the temperature detector will be in charge of converting the impinging radiation into a electric signal to be interpreted later on.

There are two classes regarding their physical working principle. On the one hand there are *thermal detectors*, whose electrical response is proportional to the absorbed energy because it changes the electrical properties of the detector due to a temperature modification of the detector itself. Meanwhile, in the case of *photon detectors*, the electrical response is proportional to the number of absorbed photons that interact with the electrons of the surface of the detector.

According to the data sheet of the IR scanner, the detector is made of Indium Antimonide (InSb), which is a photovoltaic material able to generate electric current when subjected to IR radiation. If the energy of the incident photon (e) is larger than the energy required for quantum level change (E_{gap}), the photon can excite electrons and change their energy state.

Returning to the Equation 4-2 and equating for λ,

$$\lambda_o = \frac{\hbar \cdot c_o}{E_{gap}} \tag{4-7}$$

one can see that there exists a maximum wavelength, for which the gaps between energy levels are so low that no transition occurs.

The detector of this scanner is designed to work in an spectral range going from 3.0 through 5.0 μm, under broadband conditions in the spectral range 15-5.0 μm.

It is known that the energy required for quantum level change decreases if the detector temperature does, because for low temperatures the electrons have such a low energy that remain in the valence band without conducting. This way, the action of low energy photons is able to stimulate the movement of electrons to the conductive band. For this reason, a cooling system will be needed.

4.6 Cooler.

For the reasons explained in the previous point, a cooling system is needed in order to increase the signal-to-noise ratio of the data acquisition process and/or decrease E_{gap}.

During the years, several systems have been designed to accomplish this task. For the case of the FLIR SC4000 MWIR, one encounters a *stirling closed cycle cooler*. These coolers are based on causing a working gas to undergo a stirling cycle which consists of 2 constant volume processes and two isothermal processes. Devices consist of a compressor pump and a displacer unit with a regenerative heat exchanger, known as a *regenerator*.

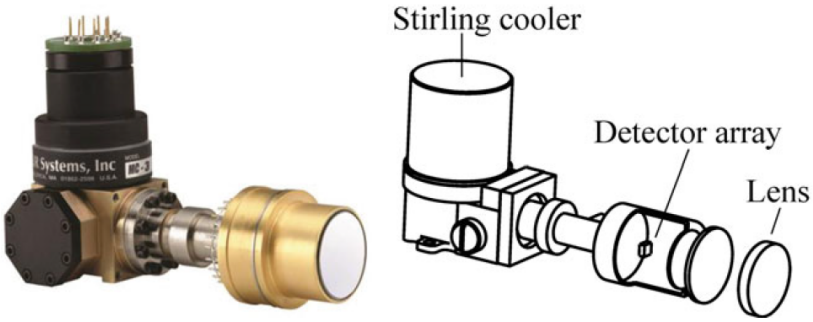

Figure 4-9: Stirling cooler with the detector array (Courtesy of FLIR Systems, Inc.) [3]

4.7 IR Scanner Performance

There are several features and variables to measure the performance of the IR scanner. According to the data sheet:

- *Thermal sensitivity* ($< 18mK$ at ambient temperature). This feature is generally expressed in terms of the mean Noise Equivalent Temperature Difference (NETD), which is the standard deviation of the random noise averaged over all pixels of a black body scene [20].
- *Spatial resolution*. Is the ability of the scanner to measure surface temperatures of small objects. FLIR SC4000 MWIR has a spatial resolution of 320(H)x256(V) pixels, having each pixel a pitch of 30x30 μm.

- *Acquisition frequency*: This feature is related to the detector response time. Although the camera can perform at 0.1 to 432 Hz, for the experiments a frequency of 10 Hz will be set.
- *Dynamic range*: For this scanner is 14 bits, and this is the number of different energy levels the signal will be composed of. As seen later, a calibration to the proper band will be needed in order to take the most of this dynamic range, so the most accurate image with differentiated temperature differences can be obtained.

4.8 IR Scanner calibration

As stated before, a calibration function will be needed to convert the radiation energy impinging the detector surface into an output signal that can be read and understood by the software.

As seen in Figure **4-10**, only a radiation flux fraction collected by the IR scanner is actually emitted by the target [9]. There are other contributions associated to the radiation emitted by the external ambient environment and the radiation of atmosphere. The effect of the external ambient environment is adding a contribution by the reflection of irradiation.

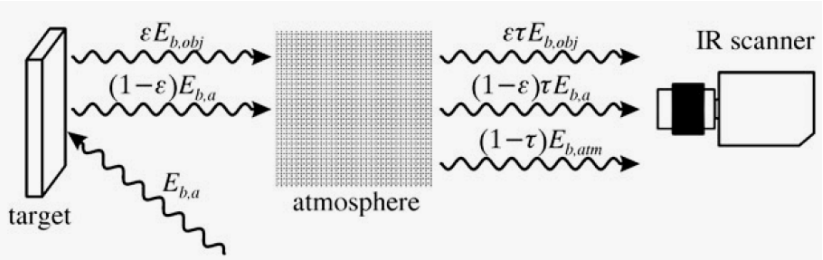

Figure 4-10: Sketch of the radiation detected by the camera [9].

The whole thing is summarized in Equation 4-8,

$$E_T = \epsilon\tau E_{b,obj} + (1-\epsilon)\tau E_{b,a} + (1-\tau)E_{b,atm} \tag{4-8}$$

The first contribution states that only a fraction ϵ of the black body radiation at the same temperature will be seen through a medium of transitivity τ. The second

and third contributions account of the effect of the ambient and the atmosphere. As stated by Carlomagno [9], the transmissivity of the atmosphere τ is assumed to be equal to unity, which simplifies Equation 4-8 to

$$U_D = \epsilon \frac{R}{e^{B/T_{obj}} - F} + (1 - \epsilon) \frac{R}{e^{B/T_{amb}} - F} \tag{4-9}$$

where U_D is the detected signal, R is a function of integration time and wavelength, B is a function of wavelength alone and F is a positive value close to 1.

There will be a mirror deviating the signal from the blackbody to the sensor and it will be difficult to account for its reflectivity and the transmitivity of the medium. For this reason, the terms in Equation 4-9 will be gathered in constants λ_1, λ_2, λ_3 and λ_4 leading to the equation that will be used for the calibration of the camera.

$$Y_{Plank} = \frac{\lambda_1}{e^{\lambda_2/T_{obj}} - \lambda_3} + \lambda_4 \tag{4-10}$$

The purpose of camera calibration is determining these constants. IR camera calibration is one of the steps to follow during this project and the process and results will be explained in Chapter 6.

Chapter 5

Experimental Set Up

The experiments took place in one of the laboratories on the Aerospace Engineering Department at the Carlos III University and a big part of the installation was mounted by Jorge Maza during his work on his bachelor thesis. Some adjustments had to be made in order to adapt his installation to the requirements of the current experiment.

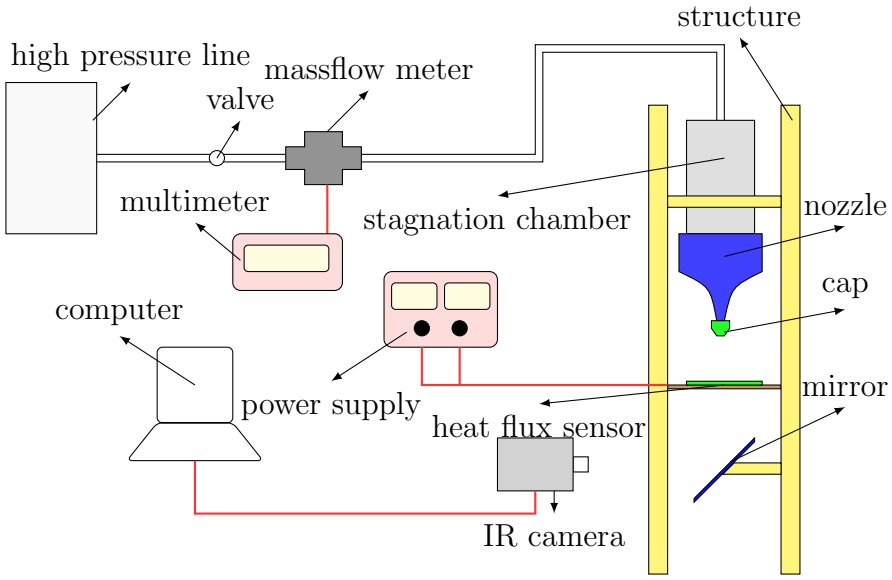

Figure 5-1: Sketch of the experimental installation.

The installation, as seen in Figure **5-1**, is composed by three groups of elements:

- The *pneumatic feeding*: these elements are in charge of the gas conduction from the compressed air source to the stagnation chamber and nozzle. A

valve controls the air coming from the compressed air source, and this one is monitored by an airflow meter for the further Reynolds number calculations.

- The *test structure*: A solid aluminum structure had to be assembled, which rigidly subjects the rest of components in order to avoid any physical error (vibrations or displacement). It will be important to allow the stagnation chamber to move vertically for being able to take measurements for different H/D values.
- The *power supply and sensing components*: These components will be in charge of putting in energy into the printed board sensor and measuring the temperature values. It is important that these components are carefully placed and oriented.

5.1 Pneumatic feeding

As stated above, the role of this segment of the installation is to connect the compressed air supply to an stagnation chamber and nozzle for the desired measurements. The compressed air supply is directly connected to the laboratory line and in order to measure the mass flow going through the application, an *mass-flow meter* had to be connected. When choosing a proper airflow meter several constraints had to be taken into account:

- A good accuracy at operation Reynolds numbers (in the range of 10000 to 40000) is desired.
- An analogical output to make easier the reading of values.
- Price.

At the end, AWM720P1 from Honeywell has selected, see Figure **5-2**. This device allows a flow range up to 200 SLPM with a response time of 6 ms. The airflow meter has to be connected to a *multimeter*, which reads a certain voltage for a given mass flow. The calibration data are given by the manufacturer and can be seen at the products data sheet. Taking into account the exit dimensions of the nozzle and room conditions, it was possible to plot a calibration curve to relate the voltage read by the multimeter with the massflow and Reynolds number of the problem.

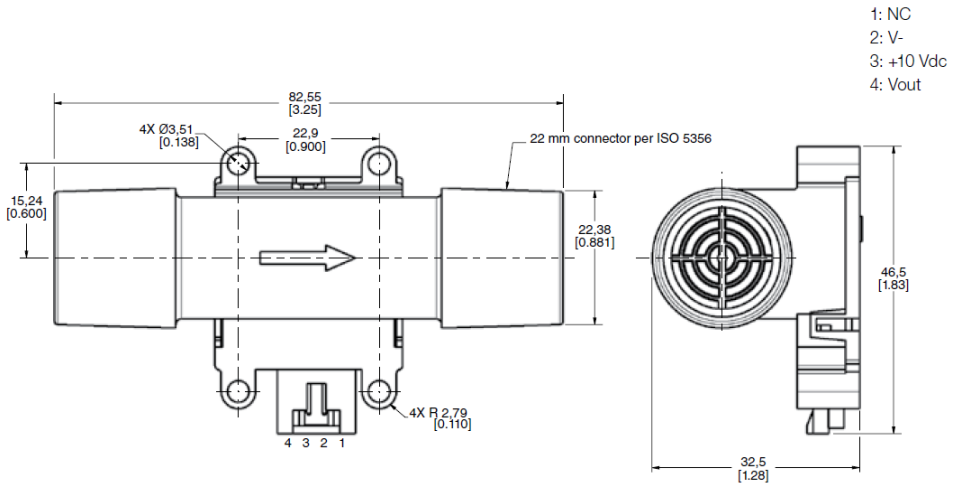

Figure 5-2: AWM720P1 Airfow meter. Image taken from product data sheet.

Because of the dimensions of airflow meter inlet and outlet, an adjustment to the available nylon tubes had to be made. For this end, a piece of thermal rubber hose, hose plug-in adapters, straight pneumatic fittings and hose clamps were used. For this type of application, where air is flowing at high velocities, special attention to air losses has to be paid, since at the hoses and pneumatic fittings, air tends escape from the circuit. During the assembly and first tests, the quantity of escaping air was a matter of concern, and for security some molding clay was added. See Figure **5-3**.

(a) Airflow meter and rubber hose.

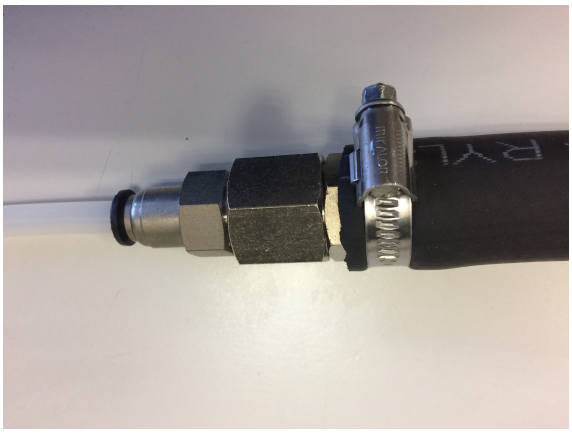

(b) Straight pneumatic fitting and hose clamp.

(c) Hose plug-in adapter covered with molding clay.

Figure 5-3: Pneumatic adjustments

5.2 Test structure

An aluminum structure to hold the components was designed, giving priority to stability and allowance to the stagnation chamber and nozzle to move vertically. It is of crucial importance that the stagnation chamber and nozzle do not vibrate and stay perpendicular to the heated thin foil sensor placed below. So, two ring clamps were used, removing two degrees of freedom and allowing only the vertical displacement of the components. See Figure **5-4**.

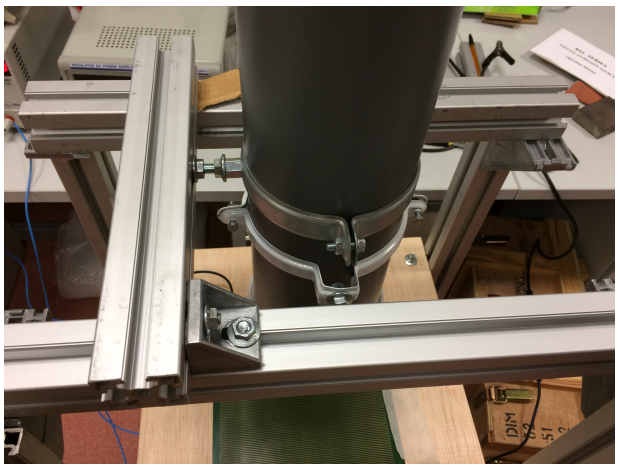

Figure 5-4: Two-ring-clamp system.

5.2.1 The stagnation chamber

The *stagnation chamber* is a cylinder connecting the nozzle and the line. Furthermore it has some other functions to fulfill:

- Supply the air stream to the nozzle.
- Assure the pressure and temperature conditions are kept nearly constant.
- Assure an homogeneous air distribution.
- Assure a one dimensional air flux.
- Subject the nozzle.

It is made up by a PVC tube for the external wall and two *internal modules*, holding *two meshes* and a *honeycomb* while isolating the airflow stream from any external agent.

The meshes are made of a regular mosquito net. There is one placed before a honeycomb to remove undesired velocity components of the airflow. There is another after the honeycomb to make sure that the flow enters the nozzle with an only axial direction.

A honeycomb is commonly used in wind tunnel applications and is placed between the two meshes to reduce swirl and turbulence. For this, 350 drinking straws were glued together, filling the whole module.

A *plug* for the top of the chamber had to be designed to allow the air to come into the chamber but not to leave it.

5.2.2 The Nozzle

One of the main components of the installation is the nozzle, conducting and expanding the flow from the stagnation chamber. Since the experiments are performed in the subsonic regime, a simple convergent nozzle is enough.

The nozzle was designed making use of the curve given by Vitoshinski theory. This expression outputs a radius distribution ($r(x)$) along an axial position (x), given the inlet and outlet radii (r_i and r_o) as well as the nozzle length (L_n).

$$r(x) = r_o \cdot \left\{ \left[1 - \left(1 - \left(\frac{r_o}{r_i} \right)^2 \right) \right] \cdot \left[1 - \left(\frac{x}{L_n} \right)^2 \right]^2 \cdot \left[1 + \left(\frac{x}{L_n} \right)^2 \right]^{-3} \right\}^{-0.5}$$

The magnitudes of the problem are:

- $r_i = 61mm$
- $r_o = 7.5mm$
- $L_n = 98.3mm$

See Figure **5-5** to visualize the inner radial profile of the Vitoshinski nozzle used during the experiments.

In Figure **5-6** the 3D printed piece is shown

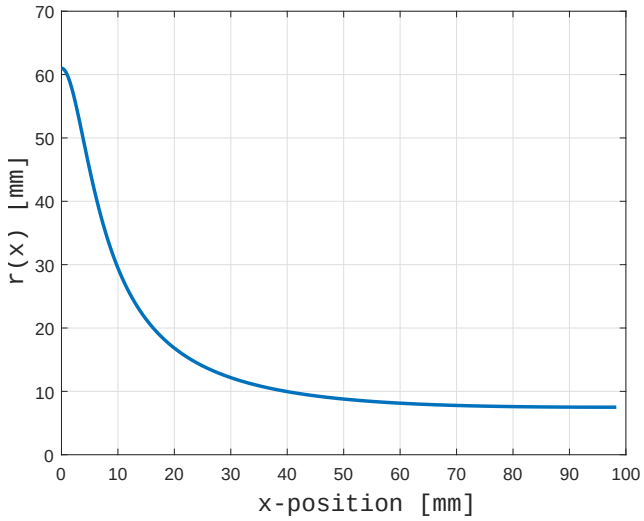

Figure 5-5: Inner Vitoshinski nozzle shape.

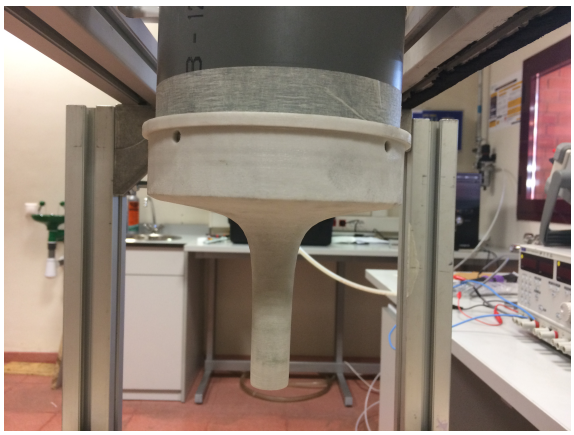

Figure 5-6: 3D printed Vitoshinski nozzle

5.2.3 Chevron Caps

For this work, several caps with chevron indentations had to be designed and 3D printed. A careful designing process had to be carried out, since the cap had to accurately fit at the end of the nozzle without breaking it, but with enough subjection so that it does not shoot off. A first basic cap without chevron indentations was designed and from there on, the rest were developed by cutting off some triangular patterns. For this work, two types of chevron indentations were tested, a positive and negative chevron type.

This way, there are two series of nozzles, each one with its own code of the form N/CXXXX. N stands for negative chevron, C for crown cap (standard chevron).

Chevron series	Number of chevrons	Chevron length [mm]	Chevron type
Circular	0	0	-
C0408	4	8	positive
C0404	4	4	positive
C0808	8	8	positive
N0408	4	8	negative
N0404	4	4	negative
N0808	8	8	negative

Table 5-1: Nozzle caps properties

The letter is followed by a series of four numbers: the two first digits indicate the number of chevrons and the last two, the chevron length in mm. In Figure **5-7**, one can see the caps printed and used during the development of the experiments. See Table **5-1** where the properties of all caps are summarized.

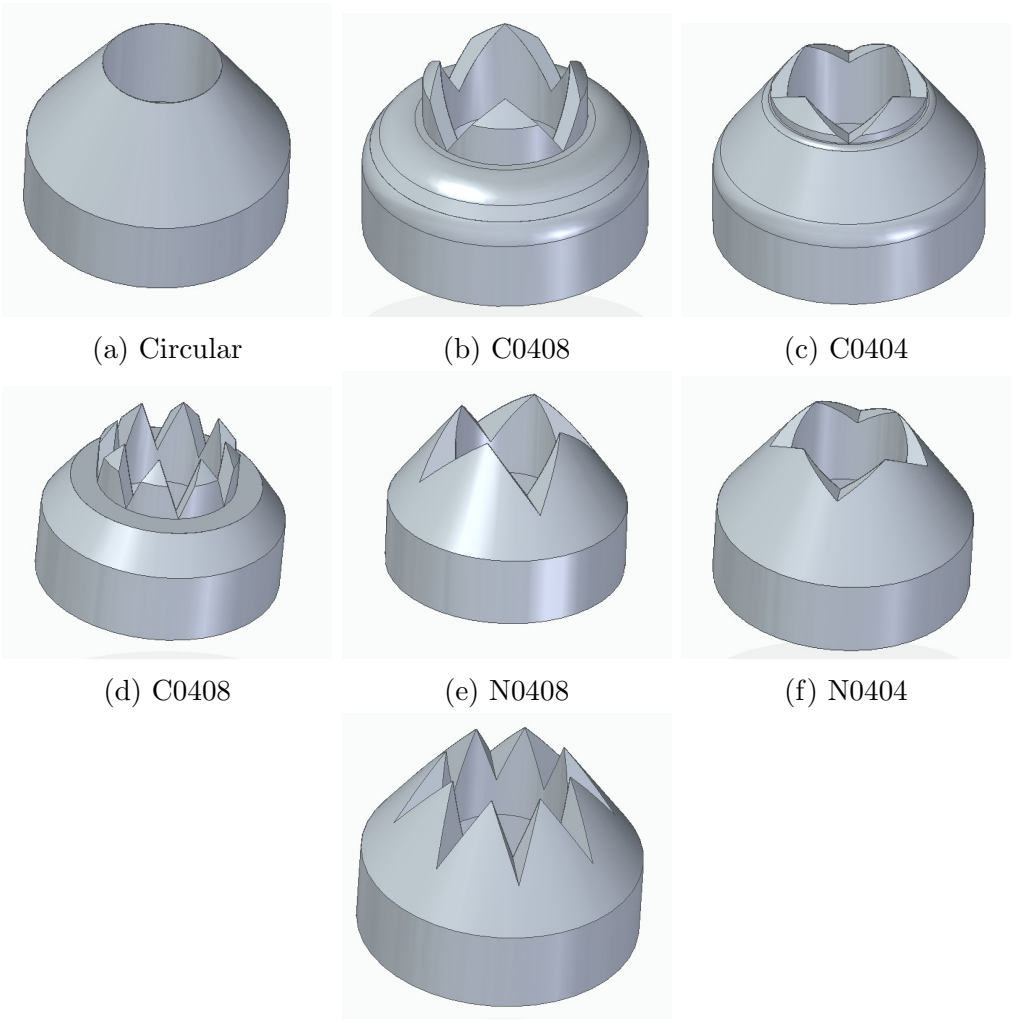

(a) Circular (b) C0408 (c) C0404

(d) C0408 (e) N0408 (f) N0404

(g) N0408

Figure 5-7: Tested chevron taps.

5.2.4 Heated foil sensor and support

As explained in Chapter 3, a printed circuit board is used as a heated-foil sensor during the experiments. The circuit chosen is made of copper tracks of 5 μ m thickness, 1 mm width and 208 mm length, with 52 tracks and a spacing between tracks of 1 mm. As seen in Figure **5-8**, the tracks are printed over a FR-4 glass-reinforced epoxy laminate sheet. It is also to be noted that an electric wire has been welded to the ends of the copper circuit in order to connect the sensor to the power source. As a support, a piece of plywood was cut and horizontally subjected to the aluminum structure.

Finally, it is important to know that over the back surface some high emissivity painting was sprayed to help the data acquisition.

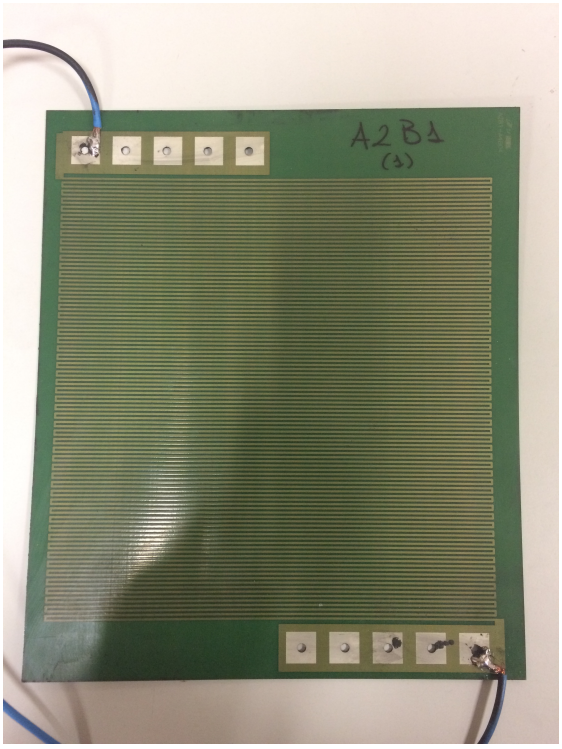

Figure 5-8: Printed circuit board.

It was very important to make sure that the nozzle completely perpendicular to the circuit, so after matching the plywood plate to the horizontal axis making use of a level, a string with a little weight was hung beside the stagnation chamber to align the perpendicular to the string.

For the first experiments, a stainless steel foil was taken as a heated-foil sensor.

This foil was placed in a methacrylate plate support with a square whole in the middle and subjected with four copper pieces and strings as described in Jorge Maza's work [27]. Thermal modeling using this sensor had already been tested in the laboratory but the dimensions of the foil lead to a pretty small regions of study. In addition, with time the copper pieces rusted and were not properly connecting to the power source. For these reasons, it was finally decided to use the printed circuit.

5.2.5 Mirror

Due to the dimensions of the camera and installation it was not possible to mount the camera to directly measure the temperatures from the thin foil sensor. For this reason, a high reflectivity mirror had to be placed at a 45º angle under the sensor, to perpendicularly deviate the radiation and direct it to the IR camera.

Figure 5-9: Mirror.

Special care had to be taken while placing the mirror and the camera, since any important deformation of the image would lead to errors in the data processing. Remember that the lateral distance from the center of the impacting jet is important, so an misproportioned image is not desired. The way to test the quantity of deformation was to place a square piece of material of known dimensions and

different emissivity than the high emissivity painting and check the dimensions in pixels measured by the camera.

5.3 Power supply and sensing

In order to supply the required energy for heating the circuit, a voltage source able to load 30 V was used. The voltage was an input, and according to the copper properties and track dimensions, a corresponding current intensity of 1.48 A came out.

As pointed out in Chapter 4, the IR camera used for this experiment was FLIR SC4000, after the calibration process described in Chapter 6.

Chapter 6

Experimental Procedure

In this chapter, a detailed explanation of the experimental procedure and data post processing is going to be explained.

6.1 IR camera calibration

As explained in Chaper 4 of this text, in order to be able to use infrared thermography as a way of measuring temperature, one needs to first calibrate the camera with a black body under conditions coherent with the ones of the experiment. In Chapter 4, was explained that the IR camera reads energy levels, which need to be transformed into temperature values by means of Planck equation. Because of the impossibility of measuring the properties of the medium and elements between the target and thermal sensor, the process of calibration resumed on finding the four constants λ_1, λ_2, λ_3 and λ_4 of Equation 4-10.

Because a black body is taken as an ideal body, instead of the printed circuit board the calibration will be performed with black body, whose temperature will be accurately regulated by a power supply. As in the actual experiment, the signal will not be directly measured by the camera, but there will be a mirror deviating it. Special care had to be taken while locating the mirror and the IR camera, because little discrepancies in the mirror angles would lead to a wrong calibration curve and incorrect temperature measurements. In order to focus the optical system, a metallic part was located close to the black body surface, taking

profit of the contrast in emissivity and temperature between the black body and the metallic part, and the lens was moved until a sharp image was obtained.

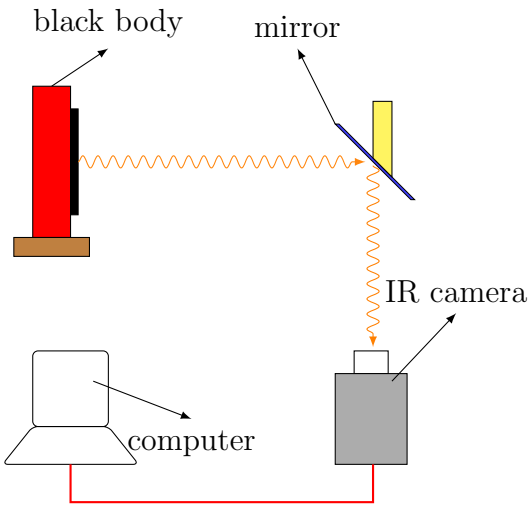

Figure 6-1: Sketch of the calibration set up.

In this case the calibration process consisted on taking measurements of the intensity numbers for different temperatures in a range from 44 through 90 °C with a step of 2 °C.

For that, a Region of Interest (ROI) of constant temperature in the center of the image was selected. The reason of selecting an area far from the edges of the blackbody is that in the proximity of the frames the read temperature tends to be slightly lower.

Making use of a controlled power supply, the blackbody was set to radiate at a desired temperature. The stabilizing of temperature for every measurement takes some time. When the temperature (and consequently the energy levels) appeared to be stabilized a recording of snapshots during 100 seconds was performed. This procedure was repeated for every temperature of interest.

Making use of Matlab codes provided by the Aerospace Department of the university, a median of the set of images taken for each temperature could be calculated and at the end, the constants for the Plank's law of radiation were obtained

In this case the constants are : $\lambda_1 = 7.1478 \cdot 10^7$, $\lambda_2 = 3214.85$, $\lambda_3 = 36.7313$ and $\lambda_4 = 2458.54$ with a correlation coefficient of 0.999027.

The calibration curve is then, according to Equation 4-10.

$$Y_{Plank} = \frac{7.1478 \cdot 10^7}{e^{3214.85/T_{obj}} - 36.7313} + 2458.54$$

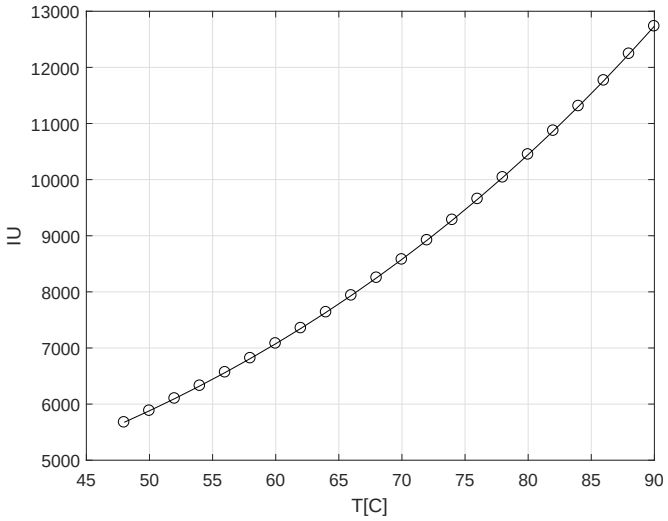

Figure 6-2: Analytic curve vs. calculated points

6.2 Massflowmeter calibration

As explained in Chapter 5, the massflow meter outputs a voltage signal to a multimeter according to the air massflow going through it. The manufacturer provided some data, relating SML and voltage, which had to be fitted into a curve using by Matlab. The result is displayed in Figure **6-3**. The result only had to be adapted later on to the dimensions of the exit nozzle for Reynolds number calculation.

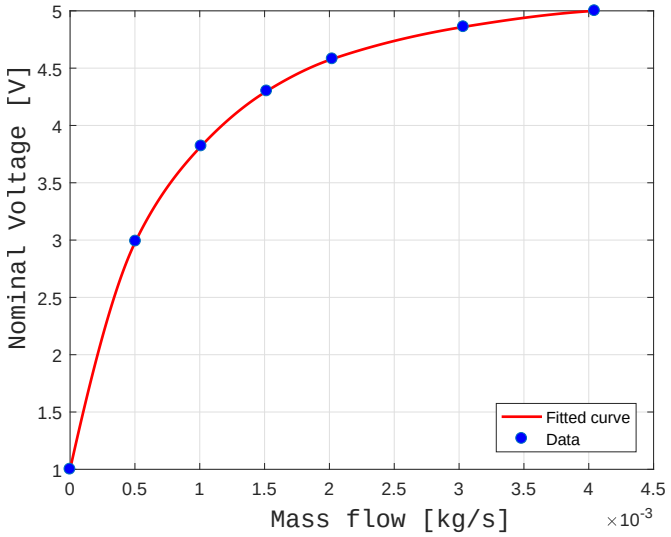

Figure 6-3: Calibration of the massflowmeter.

6.3 Data Acquisition Process

This was the longest and most tedious step of the project, since some feedback of the results had to be made and analyzed until the most appropriate arrangement of elements was found. At the end, the nozzle was pointed to the center of the circuit. All chevrons caps and for different HD distances were tested, the Reynolds number was set to 10000 for all experiments. The air source was switched on all the time.

Every measurement consisted on recording two series of frames with the power supply switched on and off. The images taken with the power supply off, were for a cold stage (used as T_{cold} during the data processing) and the images taken with the power supply on, were for a hot stage (used as T_{hot} during the data processing). Every time that data was acquired, it had to be waited for the mean of digital levels at the ROI including the plate was stabilized.

6.4 Data processing

Adapting some Matlab codes provided by the Aerospace Department of the university it was possible to process the data obtained by the IR camera. For every measurement the camera recorded a series of frames which had to be assembled and averaged together and using the calibration data obtained, transformed into temperature images. At the end two images called T_{cold} and T_{hot} were obtained.

It was also necessary to implement a model for the Joule heating and radiation and conduction heat fluxes making use of the material properties and temperatures of the ambient and surface, applying theory in Chapter 3. This way it was possible to use Equation 3-9 to find the value of the convection coefficient h, and transform it into the desired Nusselt number given by Equation 3-3. By doing this calculations over all the images, it was possible to obtain Nusselt number maps and even identify the footprint of the jet on the heated heat flux sensor.

After having visualized the Nusselt number maps, it was decided to plot calculate an azimuthal mean along the radii for every case and plot them together to see and compare the behavior in the radial direction.

6.5 Data Results Analysis and Discussion

After having processed all data, it was time so do the proper comparisons between the different designs and with the examples found in the literature, while finding a correct interpretation according to the nature of the problem.

Chapter 7

Results Analysis and Discussion.

Now, it is time to display some results and make some discussion. A comparison of the results and discussion according to theory and literature is going to be made. Important features here are going to be values of the Nusselt number and their distribution. This last feature is going to be seen by studying the jet footprint on the hot surface and azimuthal mean along the radii.

First, a description of results for the basic rounded nozzle is going to be made, in order to validate the results with other studies already made.

Then, while distinguishing the effect of having a positive negative nozzle, a comparison changing the number of chevrons and chevron length is going to be made.

At the end, conclusions of the whole analysis are going to be extracted.

7.1 Circular nozzle.

In Figure **7-1**, the Nusselt maps for the circular chevron cap, see Figure **5-7**a, at different nozzle to plate distances are displayed. The circular footprint can be easily seen and as expected from the theory, it gets narrower as the nozzle exit is placed further away from the plate.

Figure **7-2** can be compared to Figure **2-7** in the sense that for H/D of 2, the inner hump and the plateau of Nusselt between $x/r = 2$ and $x/r = 4$ is easily identified. Remember that this plateau coincides with the region of laminar boundary layer

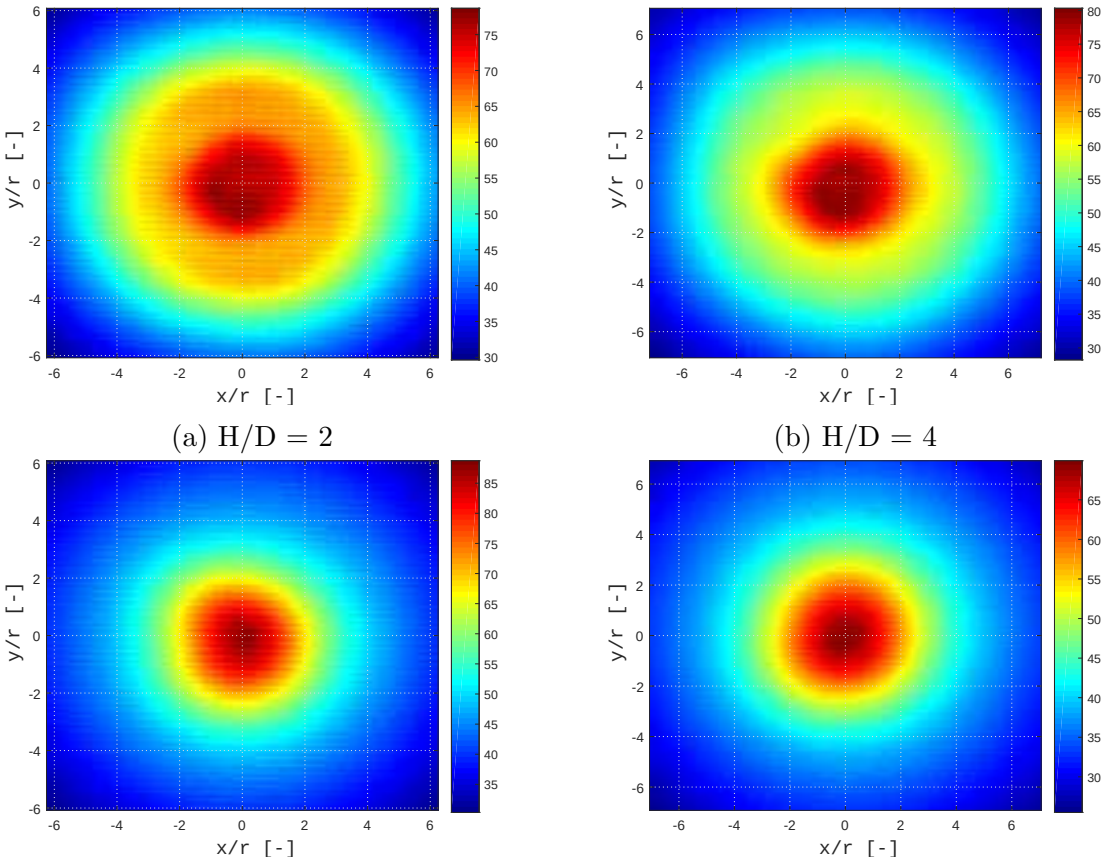

(a) H/D = 2

(b) H/D = 4

(c) H/D = 6

(d) H/D = 8

Figure 7-1: Nusselt maps for the circular nozzle at different nozzle to plate distances. Re 10000.

before entering into turbulence, as explained in Chapter 2. As the nozzle is placed further up, the shape of the radial Nusselt number mean curve resembles more a Gaussian bell, which reaches its maximum at H/D of 6. The reason for this is maximum is found when looking at the entrainment of the quiescent fluid into the shear layer of the jet. As the shear layer broadens (as explained in Chapter 2) entrainment occurs giving way to the Gaussian shape in the axial velocity profile.

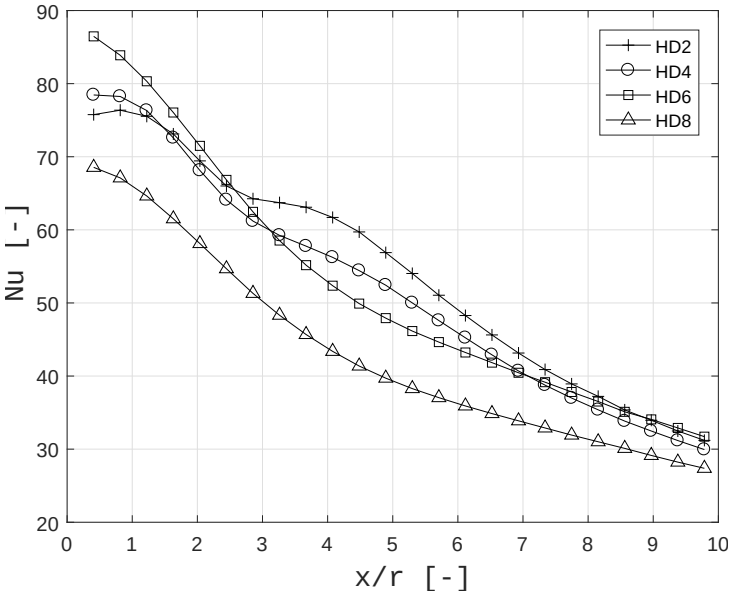

Figure 7-2: Radial mean comparison for the circular nozzle at different H/D distances. Re 10000.

7.2 Differences in chevron length.

For the caps with negative chevrons, as seen in Figure **7-3**a, one can easily differentiate the chevron notches and apexes because of the star shape of the Nusselt number footprint. Figure **7-3**b shows the same chevron cap at a H/D of 6 instead. The effect of the chevrons is less appreciated in the Nusselt number distribution, but the maximum Nusselt number reached at the center of the jet is higher. This is still correlated with the literature. For longer chevrons, comparing Figure **7-3**a and Figure **7-3**c, the star shape does not seem to change a lot, but at a first sight, for the case of negative chevrons at low H/D, it seems that longer chevrons have a negative impact on the maximum Nusselt number. At larger H/D distances, compare Figure **7-3**a and Figure **7-3**d, the effect of having longer

chevrons shows negative consequences for the maximum Nusselt number too, as long as the number of chevrons is kept to 4.

For the case of the crown caps with standard positive chevrons, at shorter distances longer chevrons show a better performance while at higher H/D distances it is observed to be the other way around. At both distances, $H/D = 2$ and $H/D = 6$, the pattern left on the plate does not change a lot and again, at a distance of two nozzle diameters, the Nusselt mark of the chevrons is to be seen.

7.3 Differences number of chevrons.

When having more chevrons, the star shape it was talked about earlier is lost and the Nusselt number footprint resembles more the one of the circular nozzle case. Looking at Figures **7-3**d, **7-3**f, **7-4**d and **7-4**f one can see that for a distance of $H/D = 6$ changing the number of chevrons does not bring a notable change neither in the pattern of the Nusselt number distribution, nor the values of the Nusselt number. On the other hand, at low H/D distances, $H/D = 2$, for the case of the negative chevron caps, the larger chevron brings a better performance, while for the positive chevron cap, the Nusselt number values behave the other way around.

7.4 Azimuthal mean analysis.

Figure **7-5** shows the result of having changed the coordinate system to a polar one and having taken azimuthal mean along the different radii.

At this point, it is important to notice that N0808 does show either the best or second best performance for these H/D values at Re 10000. In a first sight, there would not be a clear preference for negative or positive nozzles.

For a fixed distance, all Nusselt number distribution decays for all nozzles pretty much in the same way as the Nusselt number for the circular nozzle does. Even in Figure **7-5**a the hump for the inner annular peak and the plateau are conserved.

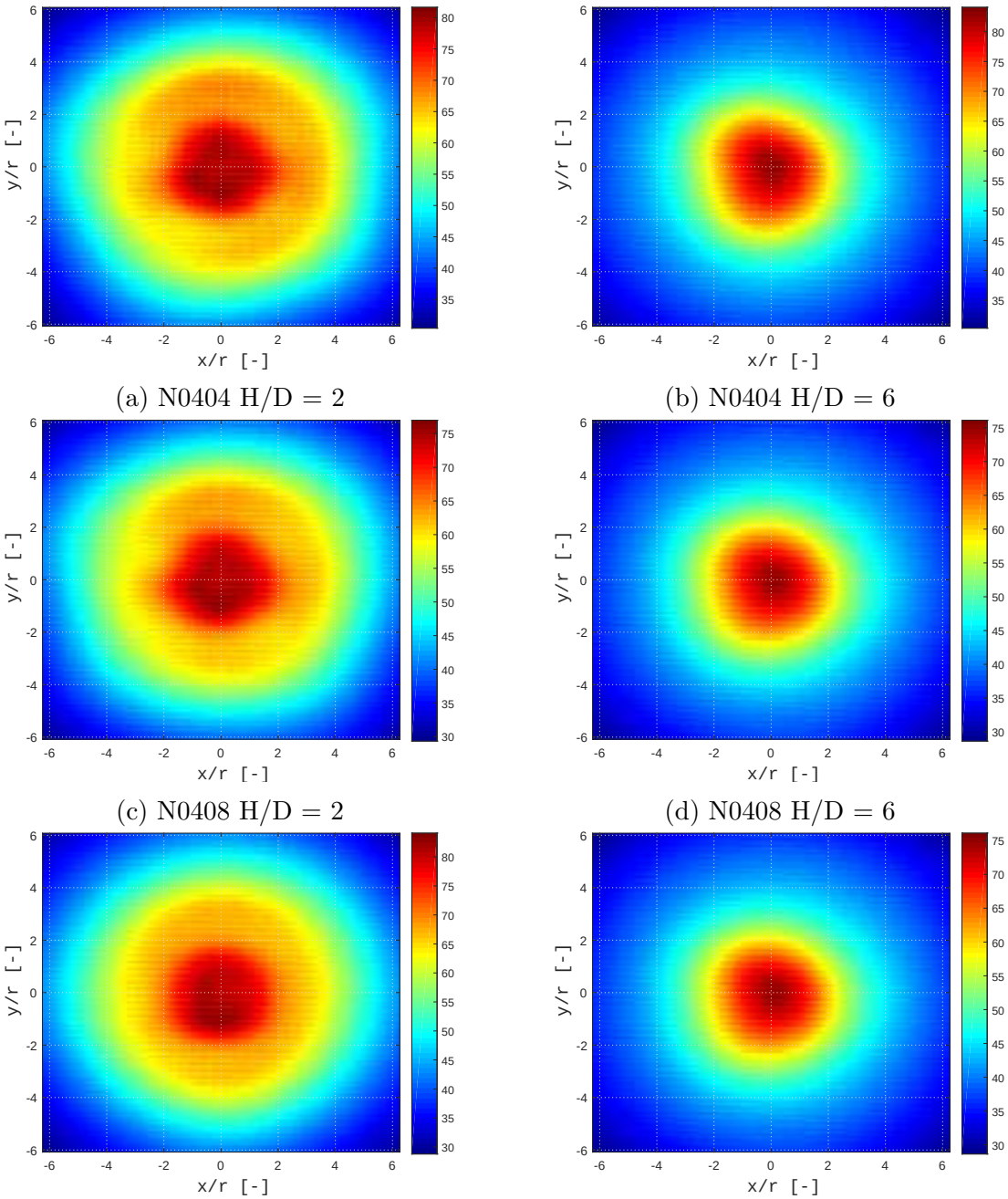

(a) N0404 H/D = 2

(b) N0404 H/D = 6

(c) N0408 H/D = 2

(d) N0408 H/D = 6

(e) N0808 H/D = 2

(f) N0808 H/D = 6

Figure 7-3: Nusselt maps for the different nozzle caps with negative chevron indentation at different nozzle to plate distances. Re 10000.

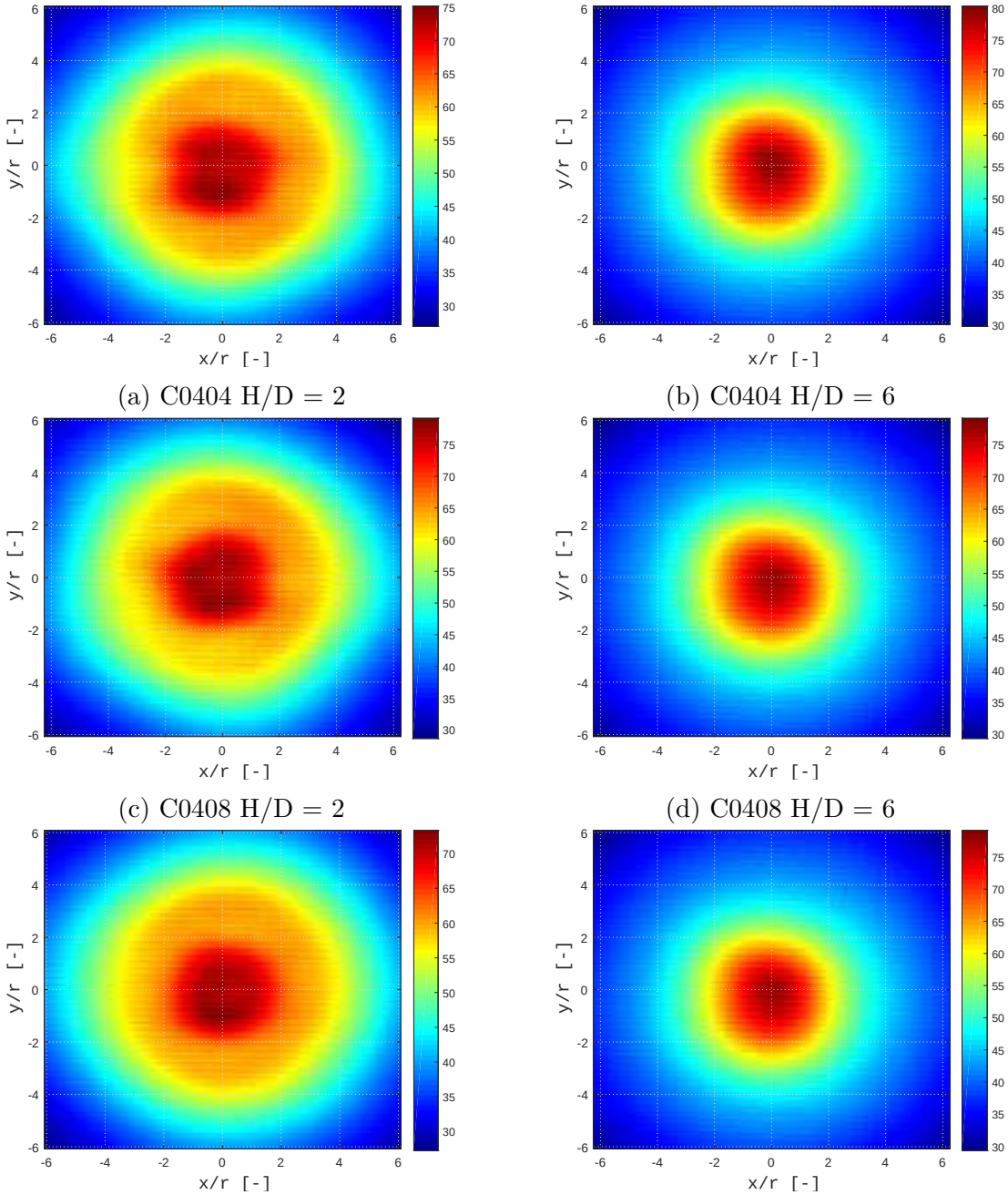

(a) C0404 H/D = 2

(b) C0404 H/D = 6

(c) C0408 H/D = 2

(d) C0408 H/D = 6

(e) C0808 H/D = 2

(f) C0808 H/D = 6

Figure 7-4: Nusselt maps for the different nozzle caps with positive chevron (crown caps) at different nozzle to plate distances. Re 10000.

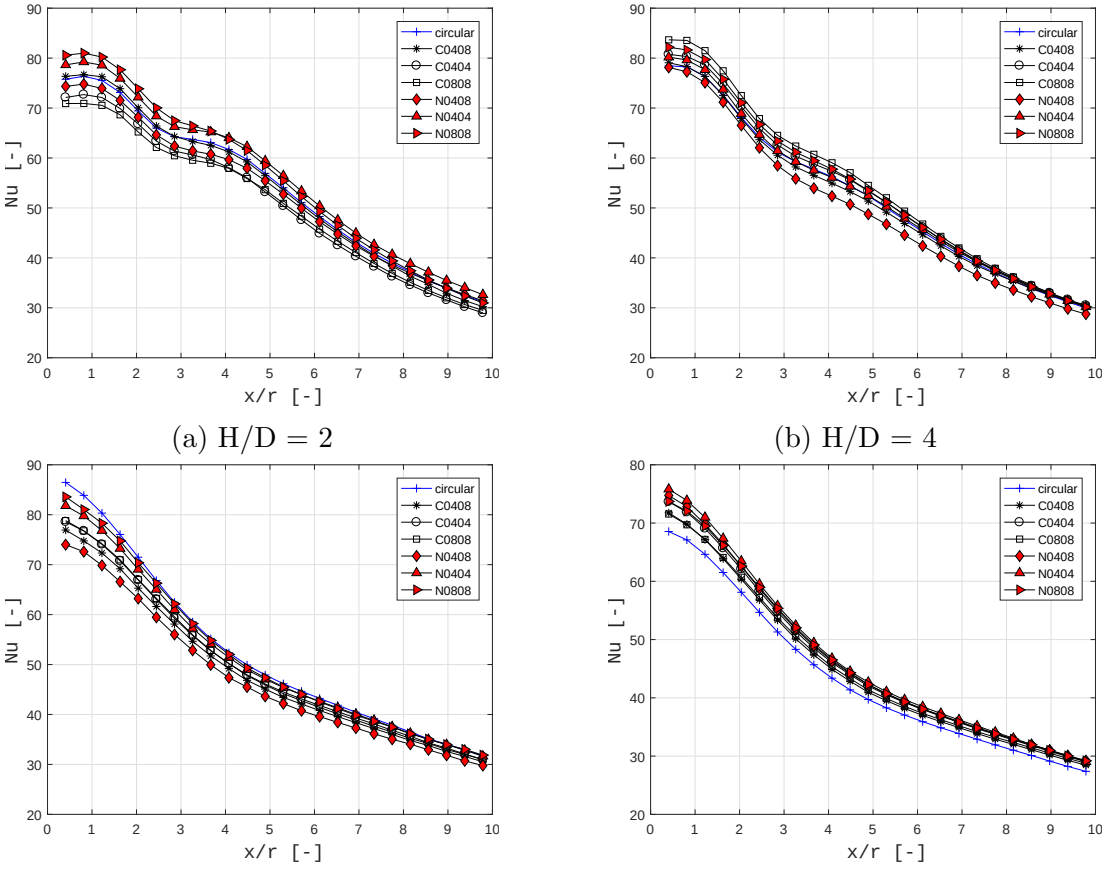

(a) H/D = 2

(b) H/D = 4

(c) H/D = 6

(d) H/D = 8

Figure 7-5: Aximuthal along the radii for different nozzle heights. Re 10000.

7.5 Uncertainty estimation.

After having analyzed the data and obtained some results, it is important to measure the uncertainty of the system to evaluate how reliable the results are. Errors are present in all measurements and are found in the uncertainty of the variables (temperatures, voltages, metric measurements...) and each variable will have its own error and uncertainty. Moffat [25] defines the error as the difference between the true value and the measured value, while the uncertainty refers to a possible value that an error can have. For the components that were bought for example, the error is given in the data sheets. The error source can be categorized as "fixed" or "random". If the source always produces the same error one talks about a fixed error, but if the error changes for every experiment a random error is referred. There can be also a variable but deterministic error, when errors that seem to be random are caused by faulty measurement techniques.

In order to quantify the uncertainty of this problem, the following algorithm was followed:

1. All variables of the problem and their errors where identified and quantified. For this, data was taken from one of the real experiments.
2. With all variables, the item of study (the Nusselt number) was taken and calculated.
3. Random perturbations contained in the error range of the variables were introduced and a new Nusselt number (accounting with the effect of the little perturbations) was calculated and stored.
4. Step 3 was repeated 10^6 times and the error of the overall problem was calculated by applying the Equation 7-1.

$$error = \frac{Nu_{std}}{Nu_{mean}} \cdot 100 \tag{7-1}$$

Where Nu_{std} is the standard deviation of the Nusselt numbers and Nu_{mean} their mean value.

For the error estimation calculations, conduction heat flux was not taken into

Parameter	Typical value (units)	Typical error ±
T_{hot}	298.1 K	0.25 K
T_{cold}	293.1 K	0.25 K
T_{amb}	293.1 K	0.1 K
ϵ	0.95 K	0.1
L	0.015 m	10^{-4} m
A	0.0437 m^2	10^{-8} m^2

Table 7-1: Control parameters and their uncertainty

account because in comparison to the summation of the rest of heat flux contributions (radiation, Joule effect and convection) the contribution is very small (<<1).

Table **7-1** was used in order to quantify the uncertainty of each parameter

The error calculated for the whole experiment is 3.89 %.

Chapter 8

Symmary and Conslusions

During the development of this projects, several thing were learned and found out. A good understanding of the literature and physics of impinging jets was needed in order to evaluate most relevant parameters for the design of the nozzle caps. Furthermore, the acquired knowledge on heat flux sensors, radiation theory and thermography was very useful during the design of the experiment and trouble shooting. Until the very last experimental configuration was obtained, many problems had to be faced an corrections had to be implemented.

The first challenge was to find a proper massflow meter which fulfilled the restrictions explained in Chapter 5 and manage the proper adaptions to the pneumatic system. During this process, knowledge on pneumatic components, fittings and standardization was obtained.

The chevron caps design was a long step as well. At first it was tough on 3D printing the whole Vitoshinski nozzle with the chevron at the end, but after several changes of design, it was decided to reuse the nozzle available at the laboratory and simply print the caps with the different chevron configurations. So, the idea of introducing negative chevrons came out. As explained in Chapter 5, it was important the the caps accurately fitted into the nozzle, since a good subjection is needed but the nozzle cannot break. Adjustments taking into account the tolerances of the 3D printer were made.

During data acquisition, several nozzle and heat flux sensor configurations were tested and feedback from the results was needed. After having checked the limitations the first heat flux sensor (thin foil sensor) it was decided to use a printed

board and by adapting the heat flux model, satisfactory results were obtained.

Last, it was seen that COMSOL is a useful tool when modeling steady state jet flows and it will open in the future opportunity for further studies in transient mode, as well as to model the whole system including the sensor cooling.

So, after a lot of adjustments and work, a good installation and efficient codes for computation were obtained. The results obtained just seem to be the beginning of a promising investigation line where other new configurations can be tested.

The carried out experiments showed an interesting response from the nozzle caps with negative chevrons. At this point it is not possible to define a preference for positive or negative chevrons, still further studies for this geometry are encouraged.

Although at $H/D = 6$, the best heat transfer performances were provided by the circular nozzle configuration, for the rest of nozzle to plate distances, chevron caps showed a better performance in terms of convective heat flux (5 to 10 % improvement). It is encouraged to keep on working with the same assembly by varying the conditions, so hopefully a good correlation between eh problem parameters can be found.

Chapter 9

Project Budget

In this section, all costs for the development of this project are going to be summarized. A first analysis of all installation components is going to be made, taking into account the different parts of the installation, and a further explanation of the electronic devices and software costs. It has to be taken into account that some of the most expensive components, as the IR camera or the black body, were not exclusively bough for this bachelor thesis, but were available in the laboratory of the Aerospace Department. In order to calculate the cost of using these elements, the depreciation during the use is going to be calculated.

If one takes a linear depreciation of the components and a life time of 5 years (60 months), one comes to the following expression for the cost of using a that component

$$cost = \frac{t_{use} \cdot price}{t_{life}} \tag{9-1}$$

For the components with a depreciation on time, in Table **9-2** are marked with an asterisk, and a precise depreciation calculation is summarized in Table **9-1**.

On the top of all this, the so called Engineering Work has to be taken into account. This cost is calculated in terms of the time devoted to each one of the tasks, the average salary of a trained engineer per hour (including taxes and social security contribution). With an average salary of 25 €/h and a total work of 300 hours during the whole project, engineering cost rise to 7500 €. In addition, transportation costs for activities like going to the warehouse have to be taken

Item	t_{use} [months]	Price €	Depreciation cost €
Power supply	4	964	64.26
Multimeter	4	800	53
Black body	0.25	10000	41.66
IR camera	4	34000	2266
Computer	4	600	40
		TOTAL	2464.92

Table 9-1: Summary of depreciation costs

Electronics and software			
Item	Quantity	Item price	Cost (€)
Electric circuit			**564.22**
Power supply *	1	964 €	64.22
Printed board	1	500€	500
Measurements and Control			**2400.66**
Multimeter *	1	800	53
Black body *	1	10000	41.66
IR camera *	1	34000	2266
Computer *	1	600	40
Software			**155.00**
Windows XP	1	120€	120.00
Matlab student license	1	35€	35.00
		TOTAL	**3119.88**

Table 9-2: Sumary of all electronic componets costs.

Installation components			
Item	Quantity	Item price	Cost (€)
Pneumatic Installation			**25.75**
Nylon pneumatic tube 8 mm	3 m	0.92 €/m	2.76
Nylon pneumatic tube 10 mm	3 m	1.02 €/m	3.06
Thermal rubber hose	0.40 m	8.83 €/m	3.53
Hose plug-in adapter	2	1.90 €	3.80
Straight pneumatic fitting	2	3.80 €	7.60
Hose clamps	4	1.05 €	4.20
Plastecine pack	1	0.80 €	0.80
Structural			**224.26**
T-slotted aluminum bars	15 m	6.51 €/m	97.65
Screews and nuts	32	2.51 €	80.32
Aluminum squads	14	3 €	42.00
Ring clamps	2	1.77 €	3.54
Plywood plate	1	0.75€	0.75
Mirror	1	35€	35.00
Stagnation chamber			**14.62**
PVC tube	1	3.12€	3.12
Modules	2	1.52€	3.04
Plug	1	1.70€	1.70
Mesh	2	0.88€	1.76
Honeycomb	1	5 €	5.00
3D printed parts			**39.14**
Vitoshinski Nozzle	70.33 cm^3	0.30€/cm^3	21.10
Nozzle caps	60.132 cm^3	0.30€/cm^3	18.04
		TOTAL	**303.77**

Table 9-3: Sumary of all material costs.

Group of costs	€
Installation components	303.77
Electronics and software	3119.88
Engineering costs	7500
Other costs	15
TOTAL	**10938.65**

Table 9-4: Sumary of total costs.

into account (15 €).

At the end, the cost of this project rises up to 10938.65 €.

Chapter 10

Regulatory Framework

This parametric study was performed at one of the laboratories of the Aerospace Department of the university, where the whole pneumatic installation was connected to a high pressure line from where the gas was coming out. The gas used during the experiments was air, but special care has to be taken when working with gases at high pressures because.

Flammable gases such as acetylene, propane and hydrogen can burn or explode under certain conditions. If flammable gases are allowed to accumulate until their concentration is between their defined Lower Explosion Limit (LEL) and Upper Explosion Limit (UEL), an explosion may occur if there is an ignition source present.

Proper ventilation is always required when working with toxic gases. Many gases are toxic and can cause serious health problems dependent upon the specific gas and its concentration, length of exposure, and route of entry.

In addition, special care in the storage and manipulation of gas cylinders has to be taken. Valves and leak checks have to be regularly undertaken.

For these and other problems, it was necessary to determine a regulatory framework to work with gases at high pressures. With the Real Decreto 379/2001 on April the 6th, the Regulations for storage of chemical products and their complementary techniques(MIE-APQ-1 to MIE-APQ-7) was approved.

Chapter 11

Future Improvements

During the development of this bachelor thesis, some points of improvement were detected, which can be taken into account further experiments.

- Add silicon to the regions where the air can leak. Controlling the Reynolds number of the problem is crucial for a proper analysis and interpretation of data and all kind of leaks have to be avoided. In order to control this, strongly tight hose clamps and Plasticine were used and this worked for Re 10000. However, for higher Reynolds, a real leak proof system should be implemented.
- Do more test at several Reynolds numbers. This can lead to hopefully a better understanding of the problem and a better validation of the results, since not much literature was found for experiments undertaken at Re 10000 only. Doing experiments at higher Reynolds number would help to also study the Reynolds number contribution to the whole problem
- The fact of experimenting with negative chevron caps brought curiosity to the researches included in the project. It would be interesting to try to understand more the flow behavior under the action of such chevrons by flow imaging techniques and more experiments. During the carried out tests, N0808 showed the best or second best Nusselt numbers.
- Combine the experiments with some multiphysics simulation software such as COMSOL, for a better understanding and validation of the results.
- Do the required changes in configuration in order to introduce an inclination

in the impingement angle and see how the results change.

Bibliography

[1] Genrikh Naumovich Abramovich, TA Girshovich, S Iu Krasheninnikov, AN Sekundov, and IP Smirnova. The theory of turbulent jets. *Moscow Izdatel Nauka*, 1984.

[2] T Astarita, G Cardone, and GM Carlomagno. Infrared thermography: An optical method in heat transfer and fluid flow visualisation. *Optics and lasers in engineering*, 44(3):261–281, 2006.

[3] Tommaso Astarita and Giovanni Maria Carlomagno. *Infrared thermography for thermo-fluid-dynamics*. Springer Science & Business Media, 2012.

[4] Bradley W Bartilson. Air jet impingement on miniature pin-fin heat sinks for cooling electronic components, January 21 1992. US Patent 5,083,194.

[5] Theodore L Bergman and Frank P Incropera. *Introduction to heat transfer*. John Wiley & Sons, 2011.

[6] John F Brausch, Bangalore A Janardan, John W Barter IV, and Gregory E Hoff. Chevron exhaust nozzle for a gas turbine engine, March 26 2002. US Patent 6,360,528.

[7] James Bridges and Clifford A Brown. Parametric testing of chevrons on single flow hot jets. *AIAA paper*, 2824:2004, 2004.

[8] Gioacchino Cafiero, Stefano Discetti, and Tommaso Astarita. Heat transfer enhancement of impinging jets with fractal-generated turbulence. *International Journal of Heat and Mass Transfer*, 75:173–183, 2014.

[9] Giovanni Maria Carlomagno and Gennaro Cardone. Infrared thermography for convective heat transfer measurements. *Experiments in fluids*, 49(6):1187–1218, 2010.

[10] Giovanni Maria Carlomagno and Andrea Ianiro. Thermo-fluid-dynamics of submerged jets impinging at short nozzle-to-plate distance: a review. *Experimental thermal and fluid science*, 58:15–35, 2014.

[11] Yunus A Cengel, Afshin Jahanshahi Ghajar, and Hsiaokang Ma. *Heat and Mass Transfer: Fundamentals & Applications, 4e*. McGraw-Hill, 2011.

[12] Kyo Sung Choo and Sung Jin Kim. Comparison of thermal characteristics of confined and unconfined impinging jets. *International Journal of Heat and Mass Transfer*, 53(15):3366–3371, 2010.

[13] F Cirillo and GM Isopi. Glass tempering heat transfer coefficient evaluation and air jets parameter optimization. *Applied Thermal Engineering*, 29(5):1173–1179, 2009.

[14] M El Hassan, A Meslem, and K Abed-Meraim. Vortex structures and entertainment in circular and daisy-shaped orifice jets. *HEFAT 2010*, 2010.

[15] Mouhammad El Hassan, Amina Meslem, and Kamel Abed-Meraim. Experimental investigation of the flow in the near-field of a cross-shaped orifice jet. *Physics of Fluids*, 23(4):045101, 2011.

[16] Robert Gardon. Heat transfer between a flat plate and jets of air impinging on it. *Int. Dev. Heat Transfer (ASME)*, pages 454–460, 1962.

[17] Fernando F Grinstein. Vortex dynamics and entrainment in rectangular free jets. *Journal of Fluid Mechanics*, 437:69–101, 2001.

[18] Puneet Gulati, Vadiraj Katti, and SV Prabhu. Influence of the shape of the nozzle on local heat transfer distribution between smooth flat surface and impinging air jet. *International Journal of Thermal Sciences*, 48(3):602–617, 2009.

[19] Jundika C Kurnia, Agus P Sasmito, Peng Xu, and Arun S Mujumdar. Performance and potential energy saving of thermal dryer with intermittent impinging jet. *Applied Thermal Engineering*, 113:246–258, 2017.

[20] P Levesque, P Brémond, J-L Lasserre, A Paupert, and DL Balageas. Performance of fpa ir cameras and their improvement by time, space and frequency data processing: Part i-intrinsic characterization of the thermographic system. *Quantitative InfraRed Thermography Journal*, 2(1):97–112, 2005.

[21] Steven Martens. Jet noise reduction technology development at ge aircraft engines. *ICAS Paper*, 842, 2002.

[22] Holger Martin. Heat and mass transfer between impinging gas jets and solid surfaces. *Advances in heat transfer*, 13:1–60, 1977.

[23] Carosena Meola, Luigi de Luca, and Giovanni M Carlomagno. Influence of shear layer dynamics on impingement heat transfer. *Experimental Thermal and Fluid Science*, 13(1):29–37, 1996.

[24] Amina Meslem, Remy Greffet, Ilinca Nastase, and Amina Ammar. Experimental investigation of jets from rectangular six-lobed and round orifices at very low reynolds number. *Meccanica*, 49(10):2419–2437, 2014.

[25] Robert J Moffat. Describing the uncertainties in experimental results. *Experimental thermal and fluid science*, 1(1):3–17, 1988.

[26] Arun S Mujumdar. *Handbook of industrial drying*. Crc Press, 2014.

[27] Jorge Maza Pallarés. Time-resolved convective heat transfer measurements,. 2016.

[28] Anna Pavlova and Michael Amitay. Electronic cooling using synthetic jet impingement. *Journal of heat transfer*, 128(9):897–907, 2006.

[29] Hendrik Tennekes and John Leask Lumley. *A first course in turbulence*. MIT press, 1972.

[30] Zdeněk Trávníček, Lucie Němcová, Jozef Kordík, Václav Tesař, and Václav Kopeckỳ. Axisymmetric impinging jet excited by a synthetic jet system. *International Journal of Heat and Mass Transfer*, 55(4):1279–1290, 2012.

[31] Ravish Vinze, S Chandel, MD Limaye, and SV Prabhu. Local heat transfer distribution between smooth flat surface and impinging incompressible air jet from a chevron nozzle. *Experimental Thermal and Fluid Science*, 78:124–136, 2016.

[32] Daniele Violato, Andrea Ianiro, Gennaro Cardone, and Fulvio Scarano. Three-dimensional vortex dynamics and convective heat transfer in circular and chevron impinging jets. *International Journal of Heat and Fluid Flow*, 37:22–36, 2012.

[33] Daniele Violato and Fulvio Scarano. Three-dimensional evolution of flow structures in transitional circular and chevron jets. *Physics of Fluids (1994-present)*, 23(12):124104, 2011.

[34] Peng Xu, Boming Yu, Shuxia Qiu, Hee Joo Poh, and Arun S Mujumdar. Turbulent impinging jet heat transfer enhancement due to intermittent pulsation. *International Journal of Thermal Sciences*, 49(7):1247–1252, 2010.

[35] N Zuckerman and N Lior. Jet impingement heat transfer: physics, correlations, and numerical modeling. *Advances in heat transfer*, 39:565–631, 2006.